



HAL
open science

A priori test of Large-Eddy Simulation models for the Sub-Grid Scale turbulent stress tensor in perfect and transcritical compressible real gas Homogeneous Isotropic Turbulence

Alexis Giauque, Corentin Giguët, Aurélien Vadrot, Christophe Corre

► **To cite this version:**

Alexis Giauque, Corentin Giguët, Aurélien Vadrot, Christophe Corre. A priori test of Large-Eddy Simulation models for the Sub-Grid Scale turbulent stress tensor in perfect and transcritical compressible real gas Homogeneous Isotropic Turbulence. *Computers and Fluids*, 2024, 268, pp.106091. 10.1016/j.compfluid.2023.106091 . hal-04933422

HAL Id: hal-04933422

<https://hal.science/hal-04933422v1>

Submitted on 6 Feb 2025

HAL is a multi-disciplinary open access archive for the deposit and dissemination of scientific research documents, whether they are published or not. The documents may come from teaching and research institutions in France or abroad, or from public or private research centers.

L'archive ouverte pluridisciplinaire **HAL**, est destinée au dépôt et à la diffusion de documents scientifiques de niveau recherche, publiés ou non, émanant des établissements d'enseignement et de recherche français ou étrangers, des laboratoires publics ou privés.

A priori test of Large-Eddy Simulation models for the Sub-Grid Scale turbulent stress tensor in perfect and transcritical compressible real gas Homogeneous Isotropic Turbulence

Alexis Giauque^{a,*}, Corentin Giguet^a, Aurélien Vadrot^b and Christophe Corre^a

^aUniv Lyon, Ecole Centrale de Lyon, INSA Lyon, Univ Claude Bernard Lyon 1, CNRS, Laboratoire de Mécanique des Fluides et d'Acoustique, UMR5509, 36 Av. Guy de Collongue, Ecully, 69134, AURA, France

^bDepartment of Mechanical and Production Engineering, Aarhus University, Aarhus, N 8200, Denmark

ARTICLE INFO

Keywords:

Large Eddy Simulation
Turbulence modeling
Real Gas Flows
a-priori study

ABSTRACT


In this study, the focus lies on the modeling of the subgrid-scale stress tensor in the context of real gas flows. By conducting tests on perfect and dense gas configurations using six different models, the research findings highlight the superiority of gradient models over eddy-viscosity models in capturing the structural behavior of the stress tensor. However, the models' performance experiences a significant decline when considering the intricate thermodynamics of real gases. To address this challenge, dynamic models that take into account the characteristics of the flow are also tested, resulting in some improvements in the outcomes. Despite these advancements, the achieved results still fall short of being entirely satisfactory. In particular, the models fail to accurately predict the occurrence of large values of the subgrid-scale stress tensor in the real gas flow. The complex thermodynamic nature of real gases therefore significantly influences the subgrid-scale stress tensor and the outcomes of this study underscore the urgent need for continued research to advance our understanding and modeling capabilities of subgrid-scale terms in real gas flows, paving the way for statistically accurate Large-Eddy Simulations of industrial real gas flows using moderately refined grids.

1. Introduction

Since its origin in the 1960s and the seminal articles of Smagorinsky [1], Deardorff [2] and Leonard [3], Large Eddy Simulation (LES) has brought invaluable understanding to the influence of unsteady features in numerous types of turbulent flows, from the most academic ones such as channel or mixing layer flows [4, 5, 6], to industrial combustion chambers or turbomachinery flows [7, 8, 9]. LES tends to be currently used with increasingly refined grids which (i) enables the accurate description of small scales dynamics and (ii) reduces the dependence on the accuracy of the subgrid-scale turbulence modeling. The price to pay for using such highly refined grids is a computational cost of LES which remains large despite the tremendous growth of computational power during the last decades. Consequently, LES is still seldom used in the industrial community for iterative design and optimization applications. Another drawback of using highly refined grids is that it tends to promote the idea that subgrid-scale modeling becomes a matter of secondary importance. It is the authors' opinion that, on the contrary, the accuracy of subgrid-scale models should be first and foremost improved to foster the use of LES in optimization and iterative design procedures thanks to the realization of coarse LES providing accurate statistics for the computed turbulent flows.

Additionally, LES models have been almost exclusively developed for perfect gas (PG) flows and mostly in incompressible regimes. However, LES turbulence closure models have been applied to different types of flows, in particular to transcritical real gas (RG) flows [10, 11, 12, 13] characterized by thermodynamic complexity which requires the use of more precise Equations of State (EoS). Although studies using these assumptions manage to match some aspects of experiments done at high-pressure they often fail to reproduce higher-order statistics. Furthermore, for some types of real gases, it has been shown that the interaction between thermodynamics and turbulence results in a completely different turbulent behavior, casting doubt on the validity of existing LES models in this context [14, 15, 16, 17]. Up to now, although the real gas thermodynamic features differ from those of perfect gases,

*Corresponding author

 alexis.giauque@ec-lyon.fr (A. Giauque)

ORCID(s): 0000-0002-2500-9912 (A. Giauque); 0000-0003-3107-8110 (A. Vadrot); 0000-0003-3255-510X (C. Corre)

1

turbulence closure models developed and calibrated for perfect gases are coupled with RG EoS and applied for LES of RG flows, for lack of a better option. One noticeable exception is the iterative deconvolution approach recently proposed by Schmitt et al. [18] and Zhang et al. [19].

Prior to developing a specialized LES model for transcritical RG flows, existing PG models must first be evaluated in this RG context, which is the objective of the present work. Since LES is based on the filtered Navier–Stokes equation, the turbulent spectrum is decomposed into resolved scales and subgrid scales which can either be modeled or neglected. First, all the subgrid-scale (SGS) terms emerging from the filtered Navier–Stokes equations have been quantified in the transcritical RG context by the authors [20]. Performing LES in this context leads to additional important SGS terms like the SGS pressure term. The authors confirm nevertheless that the most important SGS terms are the SGS turbulent stress tensor and the SGS internal energy flux. In the PG literature, those two terms (and especially the SGS turbulent stress tensor) have been the focus of a subgrid-scale modeling effort [21].

In the literature, the assessment of SGS turbulent stress tensor models has been done following two methods: *a priori* and *a posteriori* tests. In *a priori* tests, high-resolution 3D flow fields (usually obtained by DNS) are filtered to compute the exact SGS turbulent stress tensor which can then be compared to the predictions of the LES models (see for instance [22, 23, 24] for compressible configurations or more recently [25] for low-Mach channel flow). In the case of *a priori* tests, the correlation coefficient is one of the most often used comparison criteria [26, 27], especially in the data-driven turbulence modeling community [28, 29, 30]. Depending on the flow configuration under consideration, the performance is also evaluated by a comparison of averaged quantities such as mean velocity profiles, turbulence intensities, dissipation, or momentum thickness growth [31, 32]. For the *a posteriori* test, the model is implemented in the solver and LES is computed in actual conditions. Results are compared with experimental data displaying turbulence intensity decay [27], velocity profiles [2, 33] or spectra [34, 35].

Models can be classified into two groups based on their formulation and consequently on their performance: functional and structural models [21]. Functional modeling considers that the action of SGS scales over the resolved field is merely energetic. They thus display low correlation coefficients (about 0.2 to 0.3 [27, 29]) with the real SGS terms but are supposed to recover spectra. On the other hand, structural models are more closely correlated to exact SGS turbulent stress tensor (about 0.8 [27, 29]) but lead to numerical instabilities. They are thus always coupled with a dissipative term or a limiter.

The present work proposes an *a priori* assessment of six SGS turbulent stress tensor models (designed for PG flows) in the context of compressible PG and transcritical RG flows: three functional models [1, 36, 34] and three structural models [26, 37, 38] with their dynamic counterparts. No study exists that presents a comprehensive comparison of the *a priori* accuracy of SGS models in dense gases. It is important to note that because of their peculiar thermodynamic behavior, a certain amount of coupling is expected in dense gases between thermodynamics and turbulence. Hence a detailed study on SGS closure models that compares PG and RG is expected to help identifying which model would be most suited for RG simulations. The configuration under study to perform this evaluation is the forced homogeneous isotropic turbulence [39], which is part of an open RG filtered-DNS database composed of compressible mixing layers and a channel flow computed by the authors [39, 15, 16, 20] and made available to the community. Section 2 describes the derivation of the SGS terms arising from the filtering of the Navier–Stokes equations completed with thermal and caloric EoS. Section 3 briefly describes the Direct Numerical Simulation (DNS) used in this study. Section 4 and 5 respectively present details of the static and dynamic turbulence closure models evaluated in this study. The main results, namely the correlation rates and the statistical and spectral assessments of the models, are presented in Section 6.

2. Filtered equations and Subgrid-scale terms in the real gas context

The Navier-Stokes equations for the conservative quantities density ρ , momentum $\rho\mathbf{u}$ and density weighted total energy ρE read, using the implicit Einstein summation:

$$\begin{aligned}\frac{\partial \rho}{\partial t} + \frac{\partial(\rho u_j)}{\partial x_j} &= 0 \\ \frac{\partial \rho u_i}{\partial t} + \frac{\partial(\rho u_i u_j)}{\partial x_j} &= -\frac{\partial p}{\partial x_i} + \frac{\partial \tau_{ij}}{\partial x_j} \\ \frac{\partial \rho E}{\partial t} + \frac{\partial(\rho E u_j)}{\partial x_j} &= -\frac{\partial(p u_j)}{\partial x_j} + \frac{\partial(\tau_{ij} u_i)}{\partial x_j} - \frac{\partial q_j}{\partial x_j}\end{aligned}\quad (1)$$

with p the pressure, $\tau_{ij} = \mu \left(\frac{\partial u_i}{\partial x_j} + \frac{\partial u_j}{\partial x_i} - \frac{2}{3} \delta_{ij} \frac{\partial u_k}{\partial x_k} \right)$ the viscous stress tensor (μ being the dynamic viscosity), $E = e + \frac{1}{2} u_i u_i$ is the total specific energy and $q_j = -\kappa \frac{\partial T}{\partial x_j}$ the heat flux following Fourier's law, κ being the thermal conductivity. The viscosity μ and conductivity κ are computed using the Chung's constitutive equations [40] in the case of a real gas (see appendix C), and μ following Sutherland's law [41] when a perfect gas is considered.

Those dynamic equations are completed by an EoS describing the behavior of real gases. The calorific and thermal Martin & Hou (MH) EoS (Equations (2)) are used, with $b = v_c(1 - (-31.888Z_c + 20.533)/15)$, $k = 5.475$ and A_i, B_i, C_i numerical constants [42, 43] (see appendix D). Z_c is the compressibility factor, T_c and v_c are the critical temperature and critical specific volume, respectively and the notation $(\cdot)_{ref}$ refers to the reference state.

$$\begin{aligned}\text{MH}_T: p &= \frac{RT}{v-b} + \sum_{i=2}^5 \frac{A_i + B_i T + C_i e^{-kT/T_c}}{(v-b)^i} \\ \text{MH}_C: E_{int} &= E_{int,ref} + \int_{T_{ref}}^T c_v(T') dT' + \sum_{i=2}^5 \frac{A_i + C_i(1 + kT/T_c) e^{-kT/T_c}}{(i-1)(v-b)^{(i-1)}}\end{aligned}\quad (2)$$

Large eddy simulation consists in the filtering of equations (1). The filtering of a given quantity f results from the convolution of f with a kernel $G(x - \xi)$, as shown in Equation (3) with a Gaussian kernel. ζ is a parameter acting on the filter's selectivity, while Δ is the filter width. In the following, filtering is done using a Gaussian kernel with $\zeta = 6$ (see Garnier et al. [21]) and $\Delta = L/20$ (where L is the size of the periodic HIT box). The quantity f can then be decomposed into $f = \bar{f} + f'$, where \bar{f} is the filtered (or resolved) term and f' the residual (or SGS) term.

$$\begin{aligned}\bar{f}(x) &= \int_{\Omega} G(x - \xi) f(\xi) d\xi \\ G(x - \xi) &= \left(\frac{\zeta}{\pi \Delta^2} \right)^{1/2} \exp\left(-\zeta \left(\frac{x - \xi}{\Delta} \right)^2 \right)\end{aligned}\quad (3)$$

Filtering equations (1) and assuming commutativity between the filtering operator and temporal derivative or spatial gradient operators yields the following set of equations:

$$\frac{\partial \bar{\rho}}{\partial t} + \frac{\partial \bar{\rho} \tilde{u}_j}{\partial x_j} = 0, \quad (4)$$

$$\frac{\partial \bar{\rho} \tilde{u}_i}{\partial t} + \frac{\partial \bar{\rho} \tilde{u}_i \tilde{u}_j}{\partial x_j} = -\frac{\partial \bar{p}}{\partial x_i} + \frac{\partial \bar{\tau}_{ij}}{\partial x_j}, \quad (5)$$

$$\frac{\partial \bar{\rho} \tilde{E}}{\partial t} + \frac{\partial \bar{\rho} \tilde{E} u_j}{\partial x_j} = -\frac{\partial \bar{p} u_j}{\partial x_j} + \frac{\partial \bar{\tau}_{ij} u_i}{\partial x_j} - \frac{\partial \bar{q}_j}{\partial x_j}, \quad (6)$$

where \tilde{f} represents the Favre filtered quantity $\frac{\overline{\rho f}}{\bar{\rho}}$. Some terms (such as \widetilde{Eu}_j) are unknown in equations (4)-(6) because they involve subgrid-scale correlations, the filtered pressure (\bar{p}) or temperature (\bar{T}).

The filtered pressure \bar{p} and temperature \bar{T} are indeed unknown quantities because there is no commutativity between the filtering operator and the thermal or caloric Martin-Hou EoS (equations 2). In the following, the computable temperature and pressure are respectively denoted \check{T} and \check{P} (equations (9)-(10)): they represent the temperature and the pressure computed from the filtered conservative variables.

$$\bar{T} = \overline{\text{MH}_C(\rho, \rho u_i, \rho E)}, \quad (7)$$

$$\bar{P} = \overline{\text{MH}_T(T, \rho)}, \quad (8)$$

$$\check{T} = \text{MH}_C(\bar{\rho}, \bar{\rho} \tilde{u}_i, \bar{\rho} \tilde{E}) \neq \bar{T}, \quad (9)$$

$$\check{P} = \text{MH}_T(\bar{\rho}, \check{T}) \neq \bar{P}, \quad (10)$$

where MH_T and MH_C refer respectively to the thermal and caloric Martin-Hou EoS.

The transport coefficients are also influenced by the filtering process. $\check{\kappa}$ and $\check{\mu}$ denote respectively the conductivity and the viscosity computed from the filtered density $\bar{\rho}$ and the available temperature \check{T} . These observations eventually lead to the following set of equations [44] where all subgrid-scale terms are in bold type and labeled and resolved terms are in light:

$$\frac{\partial \bar{p}}{\partial t} + \frac{\partial \bar{\rho} \tilde{u}_j}{\partial x_j} = 0, \quad (11)$$

$$\begin{aligned} \frac{\partial \bar{\rho} \tilde{u}_i}{\partial t} + \frac{\partial \bar{\rho} \tilde{u}_i \tilde{u}_j}{\partial x_j} = & -\frac{\partial \check{p}}{\partial x_i} + \frac{\partial \check{\tau}_{ij}}{\partial x_j} \\ & - \underbrace{\frac{\partial [\bar{p} - \check{p}]}{\partial x_i}}_{\text{Pressure}} + \underbrace{\frac{\partial [\check{\tau}_{ij} - \check{\tau}_{ij}]}{\partial x_j}}_{\text{Viscous}} - \underbrace{\frac{\partial \bar{\rho} [\widetilde{u_i u_j} - \tilde{u}_i \tilde{u}_j]}{\partial x_j}}_{\text{Turbulent stress}}, \end{aligned} \quad (12)$$

$$\begin{aligned} \frac{\partial \bar{\rho} \tilde{E}}{\partial t} + \frac{\partial \bar{\rho} \tilde{E} \tilde{u}_j}{\partial x_j} = & -\frac{\partial \check{p} \tilde{u}_j}{\partial x_j} + \frac{\partial \check{\tau}_{ij} \tilde{u}_i}{\partial x_j} - \frac{\partial \check{q}_j}{\partial x_j} \\ & - \underbrace{\frac{\partial [\bar{p} \tilde{u}_j - \check{p} \tilde{u}_j]}{\partial x_j}}_{\text{Pressure work}} + \underbrace{\frac{\partial [\check{\tau}_{ij} \tilde{u}_i - \check{\tau}_{ij} \tilde{u}_i]}{\partial x_j}}_{\text{Viscous work}} \\ & - \underbrace{\frac{\partial [\bar{q}_j - \check{q}_j]}{\partial x_j}}_{\text{Heat Flux}} - \underbrace{\frac{\partial \bar{\rho} [\widetilde{Eu}_j - \check{E} \tilde{u}_j]}{\partial x_j}}_{\text{Energy flux}} \end{aligned} \quad (13)$$

Note that $\check{\tau}_{ij} = \check{\mu} \left(\frac{\partial \tilde{u}_i}{\partial x_j} + \frac{\partial \tilde{u}_j}{\partial x_i} - \frac{2}{3} \frac{\partial \tilde{u}_k}{\partial x_k} \delta_{ij} \right)$ and $\check{q}_i = -\check{\kappa} \frac{\partial \check{T}}{\partial x_i}$. The set of equations (11)-(13) is the equivalent for real gases of the "system II" used in Vreman *et al.*[22] for perfect gases. All terms within brackets are unknown. In a recent *a priori* study [20], the authors have shown that the main terms in real gas transcritical flows are:

- the SGS pressure which has long been the object of investigations by the research team of Prof. Bellan [45] in supercritical flows,
- the SGS turbulent Reynolds stress tensor ($t_{ij} = \bar{\rho} [\widetilde{u_i u_j} - \tilde{u}_i \tilde{u}_j]$) which is the main focus of the present study,
- the SGS energy flux.

3. DNS of Compressible Homogeneous Isotropic Turbulence (HIT)

In this *a priori* study, the models built from the filtered quantities are being compared with the exact quantities that need to be computed from DNS. The database used to test the models is composed of two DNS of forced

	M(kg mol ⁻¹)	T _c (K)	p _c (atm)	Z _c	T _b (K)	m(= c _v (T _c)/R)	n
FC-70	0.821	608.2	10.2	0.270	488.2	118.7	0.493

Table 1

Physical properties of the real gas [46].

Case	EoS	Mesh size	Turbulent velocity (m s ⁻¹)	Viscosity and conductivity	Domain size L (m)	Kolmogorov length η (m)
RG	MH	675 ³	20	Chung	4.587 × 10 ⁻⁶	1.72 × 10 ⁻⁸
PG	PG	675 ³	63	Suth.	6.845 × 10 ⁻⁶	3.21 × 10 ⁻⁸

Table 2

Key features of the HIT simulations.

compressible HIT that are run, one with a real gas, and a second one with a perfect gas. The real gas that is used is perfluorotriptylamine (FC-70, C₁₅F₃₃N), a Bethe-Zel'dovich-Thompson gas. The initial pressure and specific volume of the flow are respectively p_{init} = 0.9866p_c and v_{init} = 1.5733v_c, where the subscript c stands for critical values. Those conditions for FC-70 are such that the initial state is within the inversion zone where the fundamental derivative $\Gamma = 1 + \frac{\rho}{c} \frac{\partial c}{\partial \rho} \Big|_s$ is negative. This is done so that real gas effects on turbulence are maximized. The fluid's physical properties [46] are summarized in Table 1.

The flow is characterized by its Taylor Reynolds number Re_{λ_T} and turbulent Mach number which are defined as

$$Re_{\lambda_T} = \frac{\lambda_T \sqrt{\langle u'_i u'_i / 3 \rangle}}{\langle \nu \rangle}, \quad M_t = \frac{\sqrt{\langle u'_i u'_i \rangle}}{\langle c \rangle} \quad (14)$$

where $\lambda_T = \sqrt{2 \frac{\langle u'_i u'_i / 3 \rangle}{\langle \left(\frac{\partial u'_1}{\partial x_1} \right)^2 \rangle}}$ is the Taylor scale. The chosen turbulent Mach number for this case is $M_t = 0.8$.

Considering the sound velocity the Martin & Hou EoS yields at the initial thermodynamic state (RG case), such a turbulent Mach number is obtained with a turbulent velocity of 20m s⁻¹. For the Perfect Gas case (PG case), the EoS gives a turbulent velocity of 63 m s⁻¹ in order to reach the same turbulent Mach number.

The numerical domain is a periodic cube of size L. Each direction is discretized using 675 points, which leads to a computational domain of 675³ points. For such a resolution, the Kolmogorov scale η corresponds to 2.5 cells in the domain. The features of the numerical simulations are gathered in Table 2. Simulations were performed using the numerical solver AVBP [47]. This parallel code solves the full compressible Navier-Stokes equations (see Eqs 1) using a two-step time-explicit Taylor-Galerkin scheme for the hyperbolic terms based on a cell-vertex formulation [48]. The schemes provide high spectral resolution as well as low numerical dissipation and dispersion. The detailed analysis of the turbulence statistical properties and the comparison between the real and perfect gas flow cases can be found in a previous publication of the authors [39]. It must be emphasized that the statistical analysis of the reference PG and RG DNS simulations performed in [39] establishes that a statistically stationary state has been reached in both cases.

4. LES models for the SGS Reynolds stress tensor

The models studied here are gathered in Table 3. This section briefly describes each of them and refers the reader to the original publication for further details.

4.1. Eddy-viscosity models

The vast majority of the subgrid scale models is based on the eddy-viscosity approximation developed by Boussinesq [49]. This approximation, also referred as the linear Boussinesq hypothesis (LBH), assumes that the energy transfer from the unresolved to the resolved scales is analogous to the molecular diffusion of the viscous stresses. The LBH yield the following linear relation between the anisotropic SGS stress tensor and the strain rate

A priori test of LES models for the SGS turbulent stress tensor in perfect and transcritical compressible real gas HIT

tensor $\tilde{S}_{ij} = \frac{1}{2} \left(\frac{\partial \tilde{u}_i}{\partial x_j} + \frac{\partial \tilde{u}_j}{\partial x_i} \right)$:

$$t_{ij} - \frac{2}{3} \bar{\rho} k_{SGS} \delta_{ij} = -2 \bar{\rho} \nu_T \left(\tilde{S}_{ij} - \frac{1}{3} \tilde{S}_{kk} \delta_{ij} \right), \quad (15)$$

with $k_{SGS} = \frac{1}{2} (\overline{u_i u_i} - \tilde{u}_i \tilde{u}_i)$ the residual kinetic energy.

This strong assumption considerably reduces the modeling effort as it focuses on the Eddy-viscosity term ν_T . Following a simple dimensional analysis, the most natural model for the Eddy-viscosity is

$$\nu_T = (C_m \Delta)^2 F_m(\tilde{\mathbf{u}}) \quad (16)$$

where C_m is the constant of the model, Δ the width of the low-pass filter, F_m a differential operator based on the filtered velocity and homogeneous to a frequency, the subscript m corresponding to the model considered. By convention, the square of the constant is usually used and, as for the differential operator, is specific to each model. Among the various eddy-viscosity models present in the literature, three of them have been arbitrarily selected and are described in the following sections.

4.1.1. The Smagorinsky model

The first model to be developed was the Smagorinsky model [1] in 1963. It was first implemented and tested in LES simulations 7 years later by Deardoff [2]. This simple model is analogous to the mixing length model in which the characteristic length is the filter width Δ . The simplest term with the dimension of a frequency is the strain rate tensor. The model is then defined as

$$\nu_T = (C_s \Delta)^2 F_s(\tilde{\mathbf{u}}) \quad (17)$$

where $F_s(\tilde{\mathbf{u}}) = |\tilde{S}| = \sqrt{2 \tilde{S}_{ij} \tilde{S}_{ij}}$ is the norm of the strain rate tensor. C_s is the so-called Smagorinsky constant, usually taken equal to 0.165 for homogeneous and isotropic turbulence (HIT).

The Smagorinsky model is one of the simplest model to compute, but it suffers from several short-comings. One of the major draw-backs of the Smagorinsky model is its excessive dissipative behavior in laminar regions. Another limitation is that the model doesn't naturally vanish close to the walls and usually requires a damping function.

4.1.2. The Global Coefficient model (Vreman model)

Developed by Vreman [36] in 2004, the global coefficient model, is a static model computed as an alternative to the expensive dynamic models. It is based on the second invariant of the tensor $\tilde{G}_{ij} = \tilde{g}_{ik} \tilde{g}_{jk}$, with $\tilde{g}_{ij} = \frac{\partial \tilde{u}_i}{\partial x_j}$, the velocity gradient tensor.

For an isotropic filter, i.e. the width Δ is the same in all 3 directions, the invariant-based term simplifies to the invariant itself:

$$\tilde{I}_2 = \tilde{G}_{11} \tilde{G}_{22} + \tilde{G}_{11} \tilde{G}_{33} + \tilde{G}_{22} \tilde{G}_{33} - \tilde{G}_{12}^2 - \tilde{G}_{13}^2 - \tilde{G}_{23}^2 \quad (18)$$

The turbulent viscosity is expressed as

$$\nu_T = (C_v \Delta)^2 F_v(\tilde{\mathbf{u}}) \quad (19)$$

with the model constant being $C_v^2 = 2.5 C_s^2$ (i.e. $C_v \simeq 0.26$) and the differential operator $F_v(\tilde{\mathbf{u}}) = \sqrt{\tilde{I}_2 / \tilde{g}_{lm} \tilde{g}_{lm}}$.

4.1.3. The WALE model

The motivation behind the *Wall Adapting Local Eddy viscosity* (WALE) model [34] is to overcome the problems that have risen from the Smagorinsky model. The main advantage of this model is that it doesn't require any damping function or dynamic procedure (see Section 5 for more details) to vanish near walls.

The differential operator is built upon the square of the velocity gradient tensor. More precisely, the anisotropic symmetric of the tensor is considered. Let $\tilde{\mathcal{S}}_{ij}$ be this tensor, it is expressed as

$$\tilde{\mathcal{S}}_{ij} = \frac{1}{2} (\tilde{g}_{ij} + \tilde{g}_{ji}) - \frac{1}{3} \delta_{ij} \tilde{g}_{kk}. \quad (20)$$

A priori test of LES models for the SGS turbulent stress tensor in perfect and transcritical compressible real gas HIT

The constant of the model C_w is computed by assuming that the WALE model produces the same subgrid kinetic energy as the Smagorinsky model. The expressions of the model and its constant read

$$\nu_T = (C_w \Delta)^2 F_w(\tilde{\mathbf{u}}), \quad C_w = 0.5 \quad (21)$$

$$\text{where } F_w(\tilde{\mathbf{u}}) = \frac{(\tilde{\delta}_{lm} \tilde{\delta}_{lm})^{\frac{3}{2}}}{(\tilde{\delta}_{lm} \tilde{\delta}_{lm})^{\frac{5}{2}} + (\tilde{\delta}_{lm} \tilde{\delta}_{lm})^{\frac{5}{4}}}.$$

With this expression, the WALE model properly decreases as $\mathcal{O}(y^{+3})$ near a wall, with y^+ the distance to the wall in wall units.

4.2. The gradient models

Another family of models, the gradient models, does not rely on the Boussinesq approximation of Eddy-viscosity. These models instead derive from the Taylor expansion in the Reynolds stress tensor decomposition. The first to propose such a decomposition was Leonard in 1974 [50] which read

$$t_{ij} = L_{ij} + C_{ij} + R_{ij} \quad (22)$$

where L_{ij} , C_{ij} and R_{ij} are the so-called Leonard, cross-term and SGS stress tensors defined as

$$L_{ij} = \bar{\rho}(\tilde{u}_i \tilde{u}_j - \tilde{u}_i \tilde{u}_j), \quad C_{ij} = \bar{\rho}(\tilde{u}_i \tilde{u}'_j + \tilde{u}'_i \tilde{u}_j), \quad R_{ij} = \bar{\rho} \tilde{u}'_i \tilde{u}'_j. \quad (23)$$

By using a Taylor expansion of the filtered velocity, which hold for both box and Gaussian filters [26, 51], the three-terms decomposition (22) becomes:

$$t_{ij} = \frac{1}{12} \Delta^2 \bar{\rho} \frac{\partial \tilde{u}_i}{\partial x_k} \frac{\partial \tilde{u}_j}{\partial x_k} + \mathcal{O}(\Delta^4). \quad (24)$$

Gradient models, along with the similarity models which are not detailed here, are part of the so-called *structural* models. While the first eddy-viscosity, or functional, models aim at predicting the energy spectrum of the turbulent flow (i.e. the statistical properties of the SGS term), the structural SGS models focus on reproducing the local structure of SGS terms and turbulent eddies.

4.2.1. The Gradient model

The first gradient model to be developed was by Clark *et al.* [26]. For rapidly varying variables, the second term $\mathcal{O}(\Delta^4)$ can be too large to be omitted. The authors proposed the following model

$$t_{ij} = \frac{1}{12} \Delta^2 \bar{\rho} \frac{\partial \tilde{u}_i}{\partial x_k} \frac{\partial \tilde{u}_j}{\partial x_k} - 2\bar{\rho}(C_g \Delta)^2 |\tilde{S}| \tilde{S}_{ij}, \quad (25)$$

where the Smagorinsky model acts as a model for the $\mathcal{O}(\Delta^4)$ term. Due to its mixed nature, the gradient model suffers from the excessive dissipative character of the Smagorinsky model.

4.2.2. Liu gradient model

To get rid of the additional diffusivity from the eddy-viscosity part, one solution would be to simply get rid of the $\mathcal{O}(\Delta^4)$ term and only consider the gradient term $\frac{\Delta^2}{12} \frac{\partial \tilde{u}_i}{\partial x_k} \frac{\partial \tilde{u}_j}{\partial x_k}$. However, such a model appears to be unstable [52]. In 1994, Liu *et al.*[37] proposed to add a limiter c to the model to control the backscatter of kinetic energy and thus prevent instabilities. Liu gradient model is defined as

$$t_{ij} = c \bar{\rho} \tilde{G}_{ij}, \quad c = \begin{cases} 1 & \text{if } \tilde{G}_{ij} \partial_j \tilde{u}_i \leq 0, \\ 0 & \text{otherwise,} \end{cases} \quad (26)$$

where $\tilde{G}_{ij} = \frac{\Delta^2}{12} \frac{\partial \tilde{u}_i}{\partial x_k} \frac{\partial \tilde{u}_j}{\partial x_k}$ is the gradient term.

Model Type	Name	Model for t_{ij}	Model constant	
			PG	RG
Eddy-viscosity	Smagorinsky	$-2(C_s \Delta)^2 \bar{\rho} F_s(\tilde{\mathbf{u}}) \tilde{S}_{ij}$	$C_s = 0.165$	$C_s = 0.165$
	D-Smagorinsky	$-2(C_s \Delta)^2 \bar{\rho} F_s(\tilde{\mathbf{u}}) \tilde{S}_{ij}$	$C_{ds} = 0.324$	$C_{ds} = 0.302$
	Vreman	$-2(C_v \Delta)^2 \bar{\rho} F_v(\tilde{\mathbf{u}}) \tilde{S}_{ij}$	$C_v = 0.26$	$C_v = 0.26$
	D-Vreman	$-2(C_{dv} \Delta)^2 \bar{\rho} F_v(\tilde{\mathbf{u}}) \tilde{S}_{ij}$	$C_{dv} = 0.256$	$C_{dv} = 0.279$
	WALE	$-2(C_w \Delta)^2 \bar{\rho} F_w(\tilde{\mathbf{u}}) \tilde{S}_{ij}$	$C_w = 0.5$	$C_w = 0.5$
	D-WALE	$-2(C_{dw} \Delta)^2 \bar{\rho} F_w(\tilde{\mathbf{u}}) \tilde{S}_{ij}$	$C_{dw} = 0.4$	$C_{dw} = 0.372$
Gradient	Gradient	$\bar{\rho} \mathcal{G}_{ij} - 2(C_g \Delta)^2 \bar{\rho} F_s(\tilde{\mathbf{u}}) \tilde{S}_{ij}$	$C_g = 1.0$	$C_g = 1.0$
	D-Gradient	$\bar{\rho} \mathcal{G}_{ij} - 2(C_{dg} \Delta)^2 \bar{\rho} F_s(\tilde{\mathbf{u}}) \tilde{S}_{ij}$	$C_{dg} = 0.096$	$C_{dg} = 0.112$
	Liu Gradient	$c \bar{\rho} \mathcal{G}_{ij}$	NA	NA
	Mod. Gradient	$2(C_{mg} \Delta)^2 \bar{\rho} k_{SGS}(\tilde{\mathbf{g}}) \left(\frac{\tilde{G}_{ij}}{\tilde{G}_{kk}} \right)$	$C_{mg} = 1.0$	$C_{mg} = 1.0$
	D-Mod. Gradient	$2(C_{dmg} \Delta)^2 \bar{\rho} k_{SGS}(\tilde{\mathbf{g}}) \left(\frac{\tilde{G}_{ij}}{\tilde{G}_{kk}} \right)$	$C_{dmg} = 0.543$	$C_{dmg} = 0.608$

Table 3

List of the models used in this study.

4.2.3. The modulated gradient model (Mod. Gradient model)

The third model considered in this study that derives from the Taylor expansion (24) is the modulated gradient model [38]. This model was first developed as a gradient model for the atmospheric boundary layer in response to the limitations of the eddy-viscosity models.

The authors proposed a model based on the gradient term $\tilde{\mathcal{G}}$ and the SGS kinetic energy k_{SGS} that reads:

$$t_{ij} = 2(C_{mg} \Delta)^2 \bar{\rho} k_{SGS}(\tilde{\mathbf{g}}) \left(\frac{\tilde{G}_{ij}}{\tilde{G}_{kk}} \right) \quad (27)$$

Assuming a local equilibrium between energy production and dissipation, the SGS kinetic energy is obtained as

$$k_{SGS}(\tilde{\mathbf{g}}) = \begin{cases} 4\Delta^2 \left(-\frac{\tilde{G}_{lm}}{\tilde{G}_{kk}} \tilde{S}_{lm} \right)^2 & \text{if } \tilde{\mathcal{G}}_{ij} \partial_j \tilde{u}_i \leq 0, \\ 0 & \text{otherwise.} \end{cases} \quad (28)$$

where the same limiter as for Liu's gradient model is used.

5. Dynamic models

5.1. The Germano identity

The models seen above are implemented using an arbitrary constant, empirically defined for each flow configuration. In order to improve the models, one can consider a constant that is not only configuration-dependent, but also space and time-dependent. This constant C_d can be computed with the following dynamic procedure developed by Germano *et al.* [53].

Let's first consider a second filter, called *test* filter, under the notation \hat{f} , of width $\hat{\Delta} = 2\Delta$, Δ being the width of the *grid* filter \bar{f} . When using the composition of those two filters on the momentum equation, the SGS stress tensor becomes

$$T_{ij} = \widehat{\widehat{\rho u_i u_j}} - \frac{1}{\widehat{\widehat{\rho}}} \widehat{\widehat{\rho u_i}} \widehat{\widehat{\rho u_j}}. \quad (29)$$

This tensor can easily be related to the grid level SGS stress tensor by the following relation

$$T_{ij} = \mathcal{L}_{ij} + \hat{t}_{ij} \quad (30)$$

with

$$\mathcal{L}_{ij} = \overline{\widehat{\rho u_i u_j}} - \widehat{\rho u_i} \widehat{\rho u_j} / \widehat{\rho}. \quad (31)$$

The tensor \mathcal{L}_{ij} is called the resolved turbulent stress tensor, which physically corresponds to the contribution of the largest unresolved motions to the residual stresses. In the specific case where $\widehat{\Delta} = \Delta$, the resolved stress tensor becomes $\mathcal{L}_{ij} = \overline{\widehat{\rho u_i u_j}} - \overline{\widehat{\rho u_i}} \overline{\widehat{\rho u_j}} / \overline{\widehat{\rho}}$, which is the modified Leonard stress from Germano's decomposition of the turbulent stress tensor [54]. This second decomposition was proposed as an improved Leonard decomposition from (22) to correct the lack of Galilean invariance for the featured terms [55].

$$\begin{aligned} \tau_{ij} &= \mathcal{L}_{ij} + C_{ij} + \mathcal{R}_{ij} \\ \mathcal{L}_{ij} &= \overline{\widetilde{u_i u_j}} - \widetilde{u_i} \widetilde{u_j}, \quad C_{ij} = \overline{u_i' u_j'} + \overline{\widetilde{u_i} \widetilde{u_j'}} - \overline{\widetilde{u_i} \widetilde{u_j}}, \quad \mathcal{R}_{ij} = \overline{u_i' u_j'} - \overline{\widetilde{u_i} \widetilde{u_j'}} \end{aligned} \quad (32)$$

where \mathcal{L}_{ij} is called the *modified* Leonard stress tensor.

A relation between unknown quantities, the SGS stress tensors t_{ij} and T_{ij} , and the resolved stress tensor, which can be explicitly computed, since it only features filtered velocities and density is now given by (30). This relation is called the Germano identity and is the core of the dynamic procedure.

The general method to compute those dynamic coefficients is described below. The ratio between the test and the grid filter widths α is taken equal to 2, following the optimal value the original authors have found.

5.2. Dynamic procedure

The SGS stress tensor at the test level T_{ij} is assumed to be modeled using the same models as for t_{ij} but at the test level, with the same constant. Considering here the eddy-viscosity Smagorinsky model, it follows

$$\begin{aligned} t_{ij} &= -2\overline{\rho}(C_{ds}\Delta)^2 \left| \widetilde{S} \right| \widetilde{S}_{ij} \\ T_{ij} &= -2\widehat{\rho}(C_{ds}\widehat{\Delta})^2 \left| \widehat{S} \right| \widehat{S}_{ij} \end{aligned} \quad (33)$$

where, for the dynamic procedure, the model constant C_s has been replaced by the dynamic constant C_{ds} .

The Germano identity (30) becomes

$$\begin{aligned} \mathcal{L}_{ij} &= -2C_{ds}^2 \widehat{\Delta}^2 \widehat{\rho} \left| \widehat{S} \right| \widehat{S}_{ij} + 2C_{ds}^2 \Delta^2 \left(\overline{\rho} \left| \widetilde{S} \right| \widetilde{S}_{ij} \right) \\ &= C_{ds}^2 \times 2 \underbrace{\left[\Delta^2 \left(\overline{\rho} \left| \widetilde{S} \right| \widetilde{S}_{ij} \right) - \widehat{\Delta}^2 \widehat{\rho} \left| \widehat{S} \right| \widehat{S}_{ij} \right]}_{M_{ij}}. \end{aligned} \quad (34)$$

The constant C_{ds} can now be fully determined by use of a least squares method [56]:

$$t_{ij} = -2\overline{\rho}(C_{ds}\Delta)^2 \left| \widetilde{S} \right| \widetilde{S}_{ij}, \quad C_{ds}^2 = \frac{\mathcal{L}_{ij} M_{ij}}{M_{ij} M_{ij}} \quad (35)$$

In this form and shape, the constant C_{ds}^2 can happen to be negative. This would correspond to a reverse energy cascade, also called backscatter. The denominator of C_{ds}^2 can also become zero at some locations, and the coefficient infinite. Both of these properties have an important influence on the stability of the model. This is why it is necessary to post-process the constant in order to avoid those complications. The main method to do so is to take the ensemble average of both the numerator and the denominator [56] in the homogeneous directions. The constant now reads

$$C_{ds}^2 = \frac{\langle \mathcal{L}_{ij} M_{ij} \rangle}{\langle M_{ij} M_{ij} \rangle}. \quad (36)$$

Note that this process, while it ensures the stability of the model, largely reduces its dynamic and local character.

This dynamic procedure can be applied to all the other models listed in Section 4 featuring an arbitrary constant [57, 52, 58]. Vreman model, however, is computed by using a transport equation for the resolved stress tensor [59], which is not detailed here. The explicit expressions of the dynamic constants can be found in Appendix A.

6. Results

As mentioned in introduction, models considered in this study mostly aim at predicting the off-diagonal terms of the SGS Reynolds tensor. In addition, given the isotropic nature of the HIT used in this *a priori* study, it is chosen in the following to focus our analysis on the component t_{xy} .

6.1. 3D Correlation and Coefficient of determination (R-squared)

A very common way to analyze the quality of a model in *a-priori* analysis is to compute the Pearson correlation for the local values of t_{xy} between filtered DNS results and their modeled counterparts. Pearson correlation $\rho_{X,Y}$ is a measure of linear correlation between two sets of data (X, Y). It is the ratio between the covariance of the two variables and the product of their standard deviations; thus it is essentially a normalized measurement of the covariance.

$$\rho_{X,Y} = \frac{\mathbb{E}[(X - \mu_X)(Y - \mu_Y)]}{\sigma_X \sigma_Y} \quad (37)$$

where σ_X and σ_Y are the standard deviations of X and Y ; μ_X and μ_Y are the mean values of X and Y ; and \mathbb{E} is the expectation.

Figure 1 presents the values for the Pearson correlation obtained when taking into account a filtered 3D solution (675^3 samples) at an arbitrary time during the statistically stable regime of the HIT both for the perfect gas (PG) and real gas (RG). The first striking observation in Figure 1 is that regardless of the EoS, gradient based models show

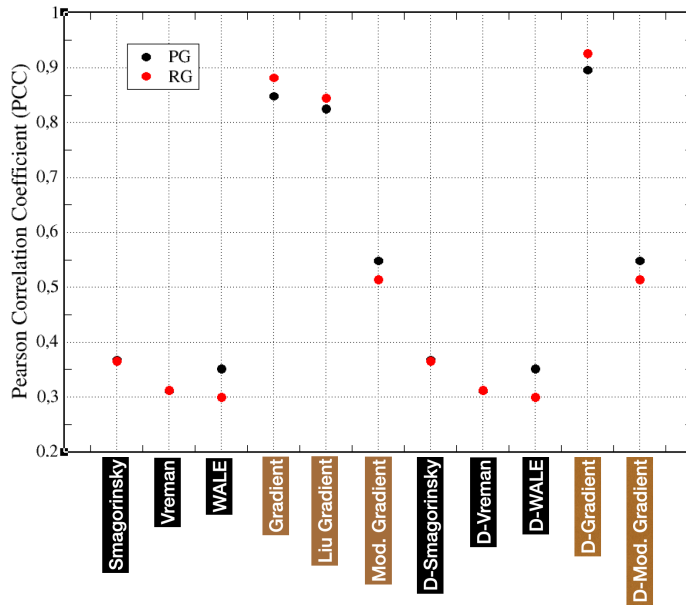


Figure 1: Pearson correlation coefficients for PG and RG cases as a function of the model used for predicting the SGS Reynolds turbulent stress tensor component t_{xy}

much larger correlation factors when compared to eddy-viscosity ones. The Gradient, Liu Gradient and D-Gradient models all achieve correlation factors larger than 0.8 which are even slightly better in the RG case when compared to the PG case. The correlation is slightly lower for the Mod. Gradient and D-Mod. Gradient models around 0.5. All Eddy-viscosity based models static or dynamic have correlation factors between 0.3 and 0.4. This result is somewhat expected, at least in the PG case [27, 29], as the gradient term is a direct representation of the SGS turbulent stress tensor and is designed to locally represent this unknown term. To be noted also, the fact that dynamic models have almost exactly the same correlation coefficient than static models. This is also expected since the Pearson correlation coefficient is a normalized measurement of the covariance which does not change with the constant of the model. The Gradient model is an exception since adopting its dynamic version reduces the dissipative term when compared to the gradient term, increasing the correlation coefficient (see Equation 25).

A more selective tool to evaluate the prediction of a model is the R^2 -score between the model and the DNS. It represents the proportion of variance of a variable Y that is explained by the variable f predicted by the model. It is defined as:

$$R^2 = 1 - \frac{\sum (y_i - f_i)^2}{\sum (y_i - \mu_Y)^2}, \quad (38)$$

If $R^2 = 1$, the prediction is exact. It is worth noting that a model that predicts a constant value equal to the mean value of Y (μ_Y) will have a R^2 -score of zero. The coefficient of determination is here computed using the DNS as the exact data set and the modeled component t_{xy} as the predictions. Since the configuration under study is isotropic with a mean flow equal to zero, the average of t_{xy} is almost zero. As a result, a model that predicts a constant null SGS turbulent stress tensor (no-model case) will have a R^2 -score of zero. Coefficients of determination are displayed in Figure 2. All

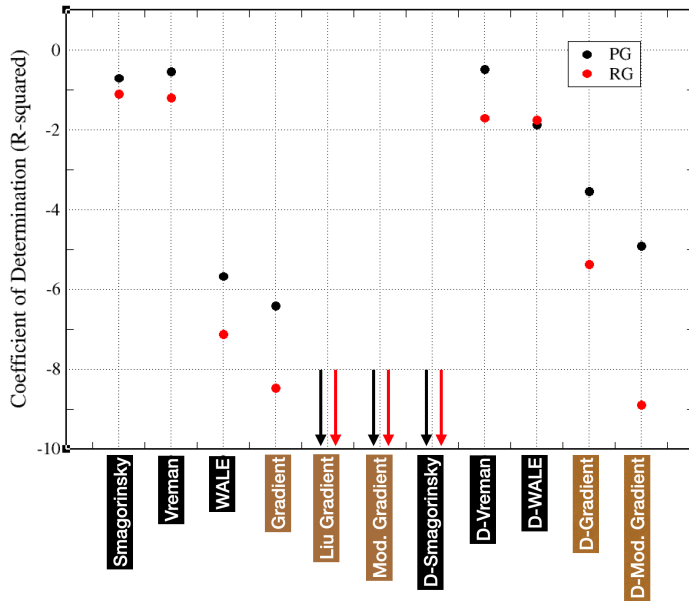


Figure 2: Coefficient of determination (R^2 -score) for PG and RG cases as a function of the model used for predicting the SGS Reynolds turbulent stress tensor component t_{xy} . Arrows correspond to determination coefficients lower than -10.

R^2 -scores are negative showing that the models make strong errors in the local determination of the SGS Reynolds turbulent stress tensor. Very large negative values of the R^2 -score especially go with a strong error in the computation of the variance of the term to be modeled.

Only the Smagorinsky, Vreman, D-Vreman and WALE models have coefficient of determination that are above -2. Those four models even achieve R^2 -scores above -1 but in the PG case only. It is worth noting that PG coefficients are always superior to RG ones. The results in this section show that Gradient models which have significant correlation levels also have very poor coefficient of determination which implies that if the trend of the SGS Reynolds turbulent stress tensor is correctly recovered, its amplitude (i.e. the variance of the term) is not correctly captured. It will be shown in the following sections that these models indeed tend to overestimate the SGS Reynolds turbulent stress tensor.

6.2. 3D Probability density function

As detailed previously, the eddy-viscosity models are best fitted to predict the functional character of the turbulence than its structural properties. A less structure-oriented way to evaluate the models' predictions is to compute the space probability density function (PDF) for the tensor component t_{xy} at hand.

Figure 3 examines the PDF of t_{xy} for the different eddy-viscosity based models as well as for the DNS solution. The x -axis is normalized with the RMS value of t_{xy} taken from the respective PG and RG DNS. The first observation from Figure 3 is the differences between the PDF of t_{xy} in the DNS that arise from the change in the EoS. Indeed, in

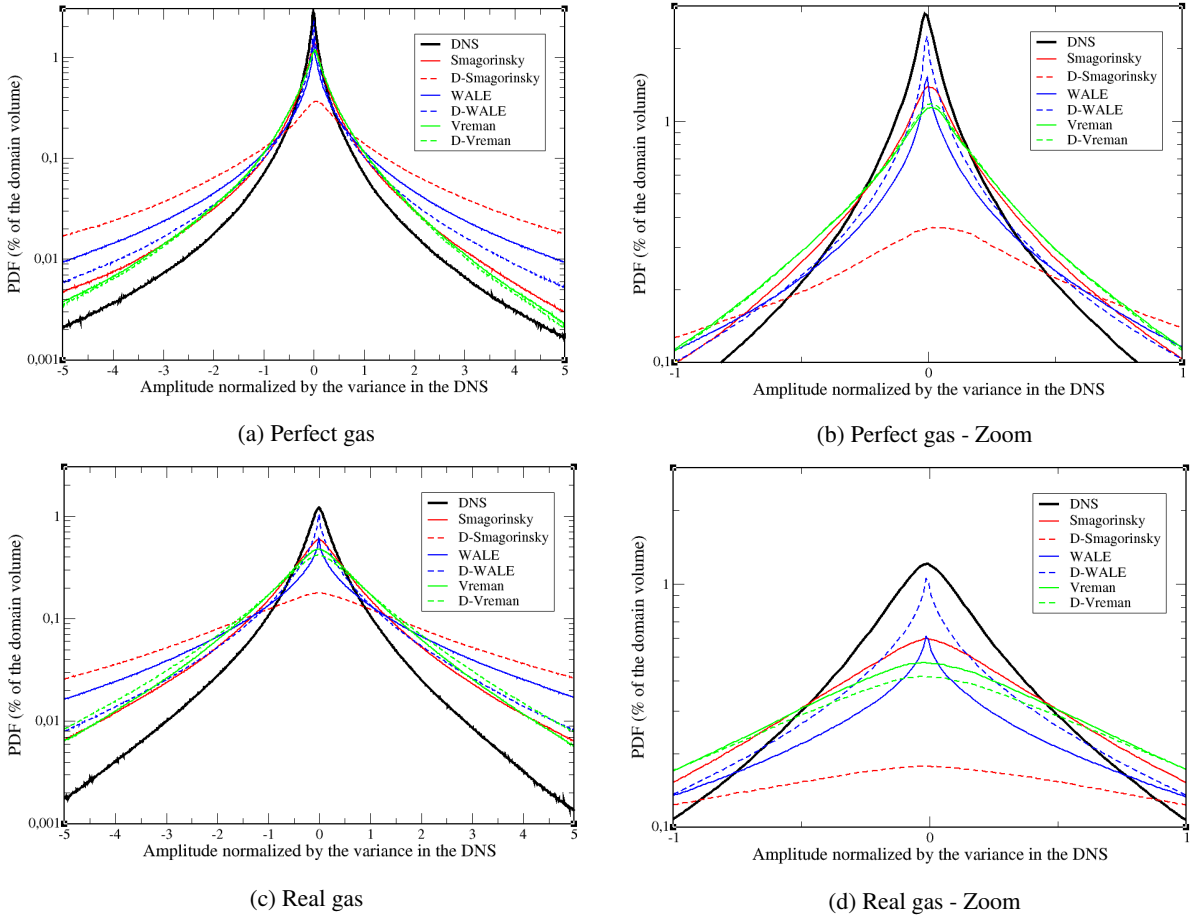


Figure 3: Eddy viscosity models : Comparison of t_{xy} PDF between models and DNS.

the RG flow, the PDF almost follows a Laplace distribution for terms smaller than the variance. This shows that the amplitude distribution could be predicted by a model following a Laplace motion description. This is quite different in the PG case in which the distribution much more closely follows the Gaussian distribution.

As far as the models are concerned, for terms smaller than the DNS variance, one should distinguish between the PG and RG cases. For the PG case, all eddy-viscosity based models (except the D-Smagorinsky model) perform fairly well and manage to reproduce quite accurately the space distribution of t_{xy} . Better than all others the D-WALE model matches the PDF in the DNS within a few percents. For large values of t_{xy} (beyond the DNS variance), a clearer ordering of the models appear with Vreman and Smagorinsky models outperforming WALE, D-WALE and D-Smagorinsky models. For the RG case, given the different shape of the PDF, no model accurately captures the shape and levels of the distribution. For moderate terms, smaller than the variance in the DNS, only the D-WALE model manages to recover the probability of occurrence of very small terms. All other models tend to underestimate this probability and over-estimate that of large terms. For terms larger than the DNS variance, this trend is confirmed. All models tend to overestimate by an order of magnitude the probability of occurrence of t_{xy} having an amplitude equal to five times the DNS variance.

Figure 4 examines the PDF of t_{xy} for the different gradient based models as well as for the DNS solution. Figure 4 clearly shows that gradient based models are not designed to reproduce statistical distributions of the SGS Reynolds turbulent stress tensor. They all show poor results regardless of the EoS. For the Gradient model, the dynamic procedure only applies to the correction term thus the difference between results obtain with the Gradient and the D-Gradient models are very close and show similar accuracy. Gradient and D-Gradient models underestimate the probability of occurrence of small values of t_{xy} below one half (PG) to one DNS variance (RG). Beyond those limits both models strongly over-estimate these probabilities. Trends are the same for Liu Gradient, Mod. Gradient and D-Mod. Gradient

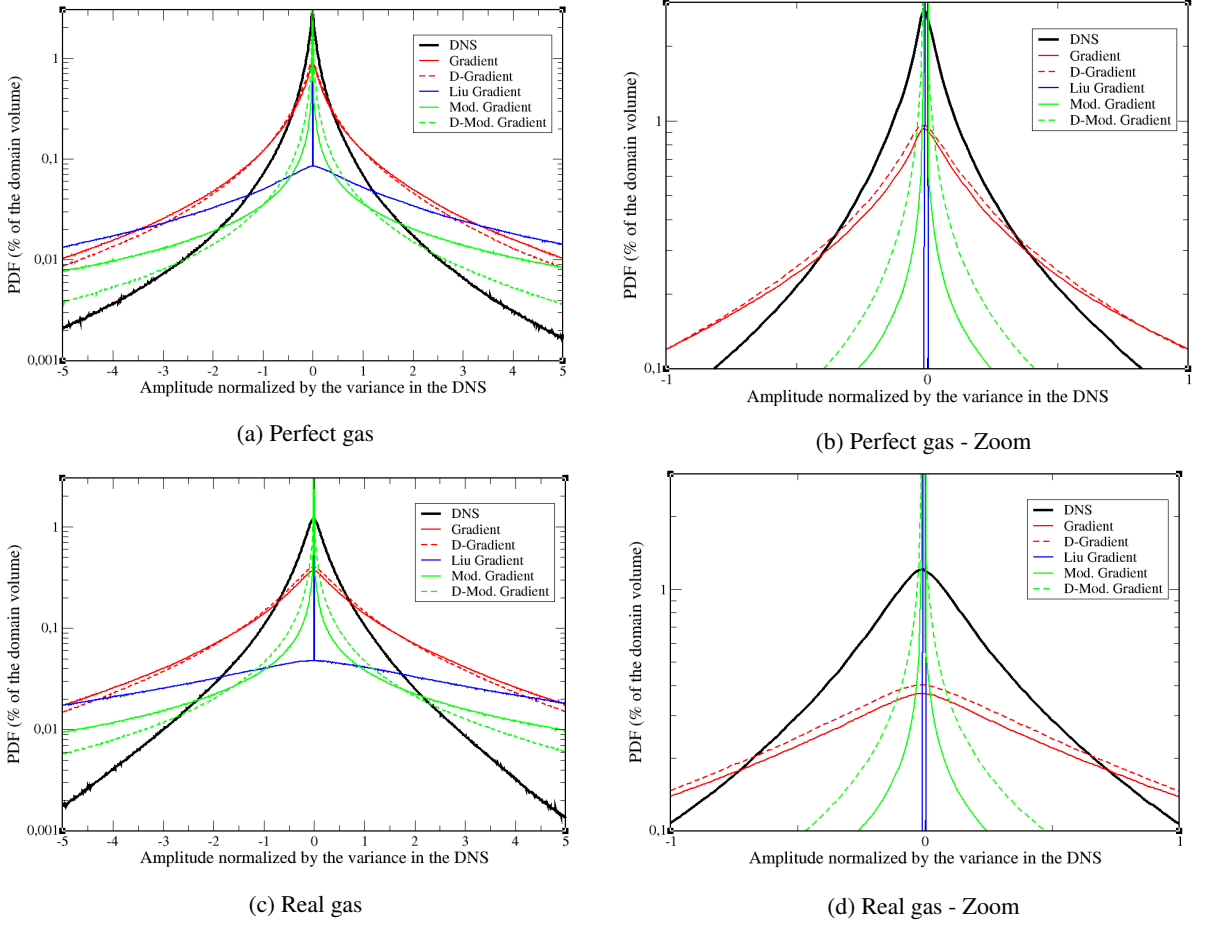


Figure 4: Gradient models : Comparison of t_{xy} PDF between models and DNS.

models. For large values of t_{xy} , the D-Mod. Gradient however shows a better behavior in the PG case when compared to the RG case. Note that the Liu Gradient PDF displays a slope break at small amplitude of t_{xy} likely because of the use of a limiter to prevent backscatter.

To better compare PDFs, Figure 5 presents the normalized L2 errors (computed using Eq 39 for $n = 0$ and $n = 1$) with respect to the DNS for the different models and EoS. As n increases, the normalized L2 error focuses more on the capability of the model to accurately predict the probability of occurrence of large t_{xy} terms.

$$L2_{err}(n\sigma) = \frac{\int_{-10\sigma}^{-n\sigma} [\text{PDF}_{\text{DNS}}(x) - \text{PDF}_{\text{model}}(x)]^2 dx + \int_{n\sigma}^{10\sigma} [\text{PDF}_{\text{DNS}}(x) - \text{PDF}_{\text{model}}(x)]^2 dx}{\int_{-10\sigma}^{-n\sigma} \text{PDF}_{\text{DNS}}(x)^2 dx + \int_{n\sigma}^{10\sigma} \text{PDF}_{\text{DNS}}(x)^2 dx} \quad (39)$$

6.3. 2D-Spectrum analysis

To further analyze functional error and gain a better understanding of the accuracy with which each model accounts for the intensity of SGS structures as a function of their wavenumber, 2D fields along an arbitrary (x, y) plane of t_{xy} are considered and compared to their DNS counterpart. Results obtained for all models and for both EoS are presented in details in Appendix B. Figure 6 presents the spectrum obtained from the considered 2D-fields for all the models. First, it can be noticed from the DNS results that the space distribution of t_{xy} is very similar between the PG and RG cases. Both cases display contents that are of significant amplitude between $5 k_{min}$ up to the filtering wavenumber (corresponding to $k = 20k_{min}$) and then quickly decrease as the wavenumber further increases. It is in that range of k that *a-priori* results should be analyzed. Indeed, if the *a priori* filtering aims to represent the grid cut-off mechanism occurring

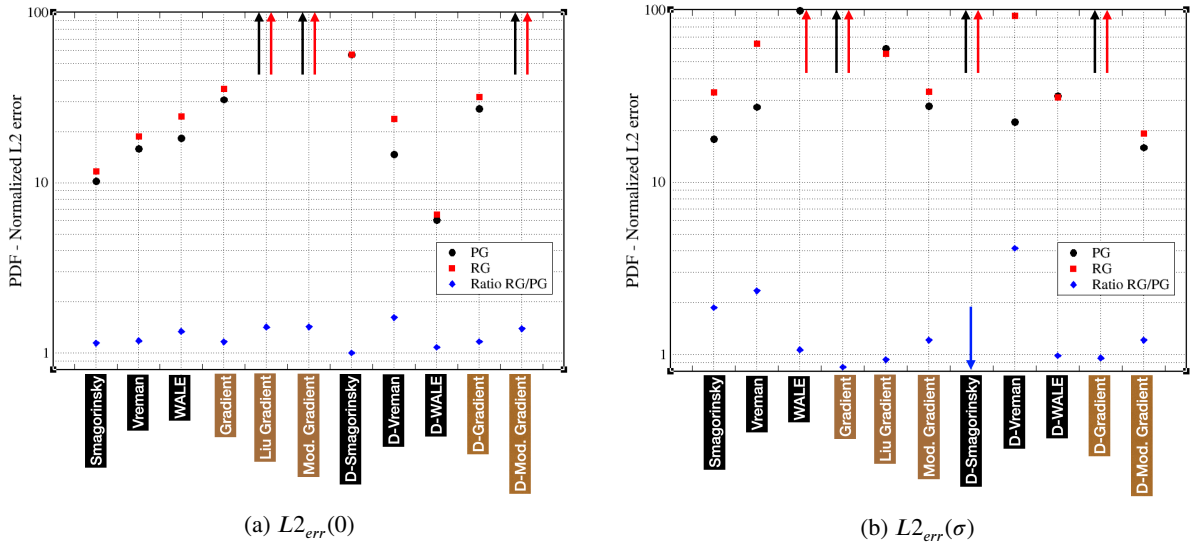


Figure 5: PDF - Normalized L2 error (in %) and Ratio of L2 errors as a function of the EoS for two different integration limits 0 (a) and σ (b) (see Equation 39). Red and black arrows respectively correspond to errors larger than 100% for the RG and PG EoS cases. Blue arrow corresponds to a ratio of the error RG over PG smaller than 0.8.

in LES, structures associated to wavenumbers larger than this cut-off wavenumber should merely be considered as artifacts of the filtering process that will not influence the result in *a-posteriori* studies. Because the numerical filter is a Gaussian filter, some energy remains at wavenumbers larger than the filtering one. To clearly identify the "resolved" and "sub-grid" scales, a vertical dotted line is present in Figure 6 at the wavenumber $k = 20k_{min}$.

When looking at the models used in this work in the PG case, it appears that the Vreman and D-Vreman models both accurately reproduce the intensity of resolved structures of t_{xy} . The Smagorinsky model comes next with a slight over-estimation of the spectrum and among static models using the linear Boussinesq hypothesis (LBH), the WALE model is the one most over-estimating the spectrum. Other Dynamic models using the LBH (D-Smagorinsky and D-WALE), all overestimate the spectrum of t_{xy} with the D-Smagorinsky model being the worst with an overestimation of more than an order of magnitude. Observing now the gradient-based models for the PG case, it appears that those models all significantly over-predict the intensity of resolved structures of t_{xy} . The application of the dynamic procedure to the Gradient or Mod. Gradient models only slightly improve the results.

Regarding the RG case and models relying on the LBH, no model accurately reproduce the resolved part of the filtered DNS spectrum. The reason is two-fold. On the one hand, the spectrum of the filtered DNS is slightly reduced before the cut-off wavenumber when compared to the PG case. On the other hand, both the Vreman and D-Vreman models predict larger values in the RG case. These two effects accumulate leading to two-fold over-estimation for the main part of the resolved spectrum in that case. The accuracy of the Smagorinsky model is unchanged between the PG and RG cases. Only the D-WALE model better predicts the spectrum when compared to the PG case. All other comments made for gradient-based models in the PG case also apply to the RG one.

As an illustration and to further understand the reported spectrum, Figures 7 and 8 for the PG and RG EoS respectively, display t_{xy} for the models providing the predictions closest to the DNS. The lack of correlation between all models and the DNS is obvious. For the PG case in Figure 7, a largely positive region at the center-left of the picture is not captured by the Vreman and D-Vreman models. Just below toward the center, a largely negative region is modeled as a significantly negative one. Yet overall, the size of the structures (positive or negative) of t_{xy} is indeed well captured.

The same lack of correlation between the models and the DNS can be observed in the RG case in Figure 8. For example, a strong positive region at the left-bottom corner ($x \approx 0.25$, $y \approx 0.2$) is missed by all models. Yet, in that case, extra filaments of positive t_{xy} are present in the modeled fields only. This is one of the possible reasons for the general overestimation of the spectrum of t_{xy} in the RG case.

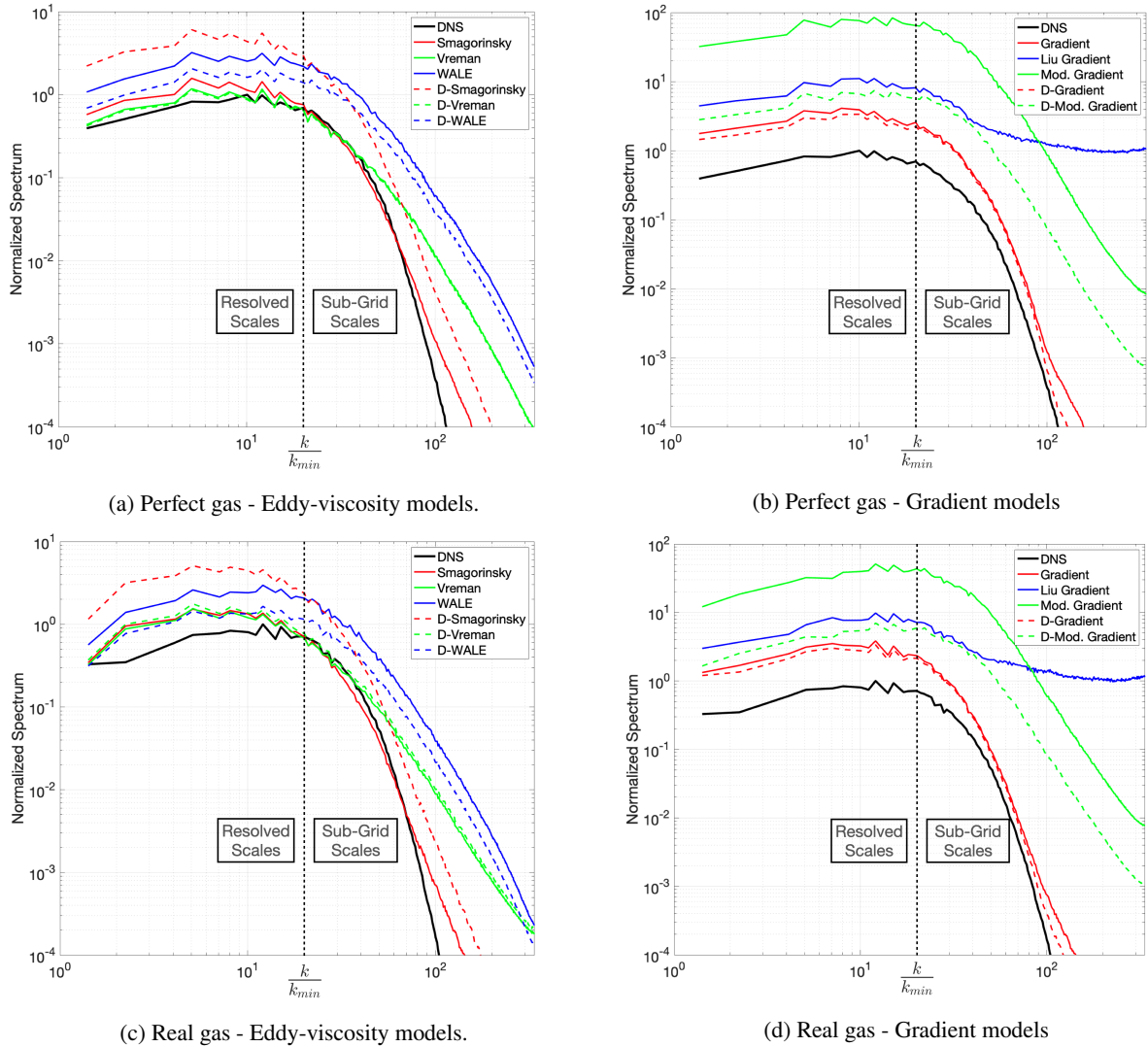


Figure 6: 2D-Spectrum of t_{xy} normalized by the maximum DNS value as a function of the wavenumber (k) normalized by the minimum wavenumber (k_{min} corresponding to the largest scale)

6.4. Summary of the results

To summarize the results and rank all studied models, Table 4 is proposed which depicts the following picture. As one could imagine, regardless of the EoS, only gradient-based models significantly correlate with the SGS Reynolds turbulent stress tensor extracted from the DNS with correlation level reaching 0.9. Yet, even for those models the dynamic of the SGS term is not well captured locally and coefficients of determination remain negative. This conclusion also applies indiscriminately of the EoS.

Regarding the capability of models to recover the PDF of the modeled term, differences between the PG and RG cases appear. The general picture is that of a worsening of the results in the RG case. Only the Smagorinsky and D-WALE models achieve fair to good results in that case. For the D-WALE model, this mostly comes from its capability to accurately predict the probability of small values of t_{xy} in the 3D field. For Smagorinsky, it comes from its better prediction of the probability of occurrence of large values of t_{xy} .

Finally, the prediction of 2D-spectrum of t_{xy} is also worsened in the EoS change. All Eddy-viscosity based models (except the D-Smagorinsky model) achieve comparable results for the RG case and all tend to overestimate the energy of large scale structures of t_{xy} .

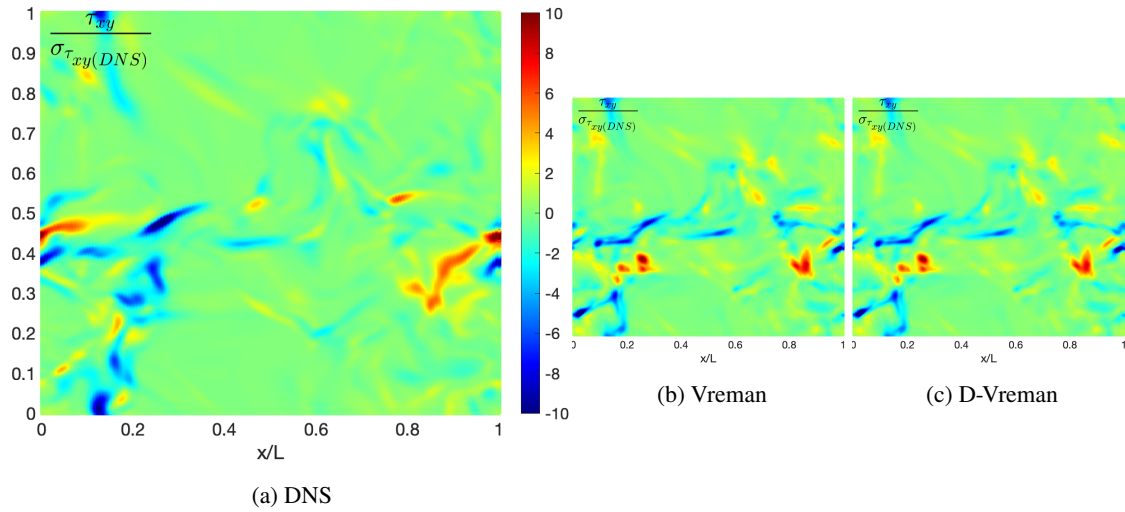


Figure 7: t_{xy} in the (x, y) plane. PG case. Turbulent SGS viscosity models providing spectrum closest to the DNS.

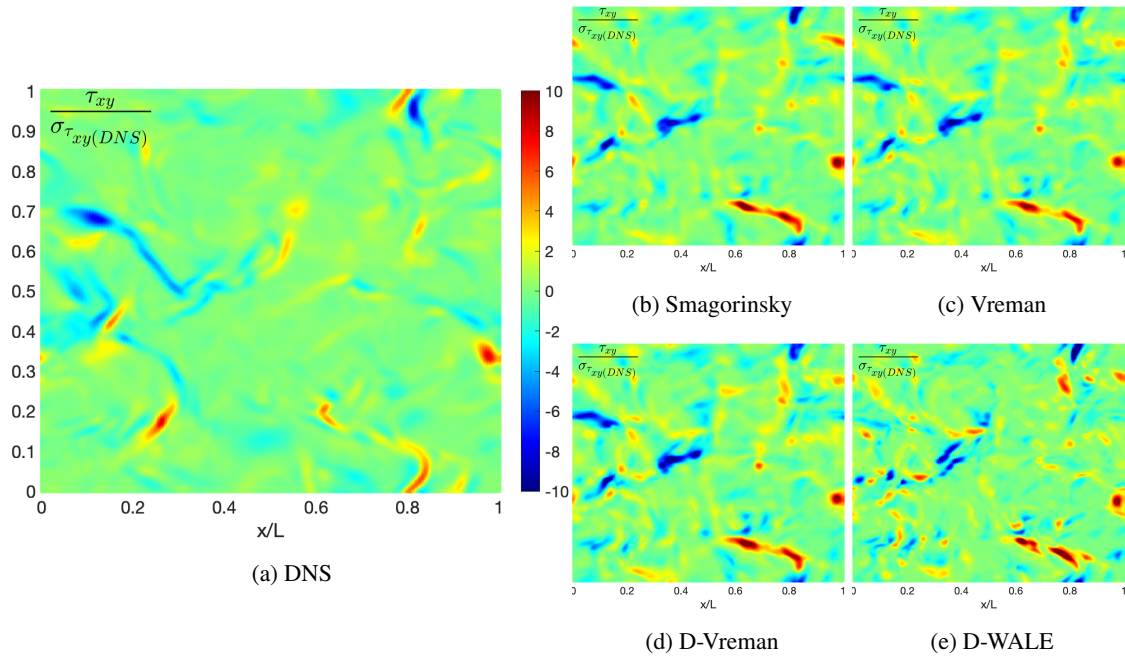


Figure 8: t_{xy} in the (x, y) plane. RG case. Turbulent SGS viscosity models providing spectrum closest to the DNS.

7. Concluding remarks

From the filtering of the Navier-Stokes equations rises a set of terms that cannot be expressed from the filtered quantities. This study has been focused on one of them, the so-called subgrid-scale (SGS) stress tensor and its modeling, in the specific case of a real gas (RG). To do so, two databases are created from the same thermodynamical state, one using the perfect gas (PG) equation of state (EoS) and the other with a RG EoS, namely the Martin-Hou EoS. Six models were considered and presented. Those models, constructed to reproduce the dynamics of a PG, are tested on both the PG and RG configurations. Considering the PG case in this study offers an element of comparison regarding the impact of a different EoS on the predictions. The models are *a-priori* compared to the DNS solution from the

Model Type	Model	Correlation		R-Squared		3D-PDF		3D-PDF large values		2D-spectrum	
		PG	RG	PG	RG	PG	RG	PG	RG	PG	RG
Eddy-viscosity	Smagorinsky	-	-	-	-	+	+	+	o	o	o
	D-Smagorinsky	-	-	--	--	-	-	--	--	--	--
	Vreman	-	-	-	-	+	+	+	-	+	o
	D-Vreman	-	-	-	-	+	+	+	-	+	o
	WALE	-	-	--	--	+	+	-	--	-	-
	D-WALE	-	-	-	-	++	++	o	o	-	o
Gradient	Gradient	+	+	--	--	o	o	--	--	-	-
	D-Gradient	+	+	--	--	+	o	--	--	-	-
	Liu Gradient	+	+	--	--	--	--	-	-	--	--
	Mod. Gradient	o	o	--	--	--	--	+	o	--	--
	D-Mod. Gradient	o	o	--	--	--	--	+	+	--	--

Table 4

Summary of the performance associated to the models used in this study.

Correlation criteria : - if ($P < 0.3$); o if ($0.3 < P < 0.8$); + if ($0.8 < P$).

R-Squared criteria : -- if ($R_2 < -2$); - if ($-2 < R_2 < 0$).

3D-PDF criteria : - if ($L_2 > 100\%$); - if ($50\% < L_2 < 100\%$); o if ($30\% < L_2 < 50\%$); + if ($10\% < L_2 < 30\%$); ++ if ($L_2 < 10\%$).

2D-spectrum criteria : + if both spectrum collapse ; o if the error is less than an order of magnitude; - or -- if the error is larger than an order of magnitude.

database. Accounting for the isotropy of the test case, this study focuses on one of the components of the SGS stress tensor : t_{xy} .

The structural performances are evaluated using the coefficients of determination with respect to the DNS. The results confirm that gradients models designed to recover the structural behavior of the SGS stress tensor perform better than eddy-viscosity ones. If Pearson correlation factors reach values larger than 0.8, R^2 scores are disappointing and worsen with RG effects. To switch focus to the functional error of the models, the PDFs of the turbulent stress tensor are computed in the DNS and compared to the modeled ones. The first observation is that of the strong difference between the PG and RG cases, the latter exhibiting PDFs significantly departing from the former. Also quite expectingly, eddy-viscosity models better recover the PDF than gradient-based models, especially for the PG case. In the RG case, none of the tested models stands out. Considering those poor results, the dynamic version of the models are implemented, in which the arbitrary constant is now built from the flow’s characteristics. They present better results when the coefficient of determination is considered, even though those results are not yet satisfactory. The study of the PDFs shows that the dynamic computation has indeed reduced the coefficient of the models, but in a too important manner for the eddy viscosity models. Further analyses of the 2D spectrum of the subgrid-scale stress tensor term t_{xy} confirm these observations.

These results indicate poor a priori performance of the SGS models for both PG and RG, with RG showing however notably poorer outcomes when predicting the extreme values of 3D-PDF. This highlights the potential influence of the complex thermodynamics of RG on the SGS stress tensor and calls for a renewed effort focusing on the specific modeling of SGS terms in RG flows. Researchers and engineers conducting LES of RG compressible flows still use today SGS models which have been designed for PG compressible flows with no specific modeling effort when applying them to RG configurations. The present study therefore also points out the need to be aware that the accuracy of these models is further reduced when applied to RG flows.

Following the a priori analysis performed in the present study, high-resolution LES of a well-documented RG flow configuration of interest for the turbomachinery community (namely the annular cascade experimentally studied in [60]) will be performed using a selection of some of the SGS models investigated here.

Acknowledgements

This work has been supported by the JCJC ANR EDGES project, grant #ANR-17-CE06-0014-01 of the French Agence Nationale de la Recherche. Simulations have been carried out using HPC resources at CINES under the project grants #A0102A07564 and #A0122A07564. The authors would also like to thank the CFD team (especially Gabriel

Model	Constant C_d	Tensors
D-Smagorinsky	$\langle \mathcal{L}_{ij} M_{ij} \rangle / \langle M_{ij} M_{ij} \rangle$	$M_{ij} = 2 \left[\Delta^2 \left(\widehat{\bar{\rho}} \widetilde{S}_{ij} \right) - \widehat{\Delta}^2 \widehat{\bar{\rho}} \left \widehat{S} \right \widehat{S}_{ij} \right]$
D-Gradient	$\frac{\langle (\mathcal{L}_{ij} - H_{ij}) M_{ij} \rangle}{\langle M_{ij} M_{ij} \rangle}$	$\begin{cases} M_{ij} = 2 \left[\Delta^2 \left(\widehat{\bar{\rho}} \widetilde{S}_{ij} \right) - \widehat{\Delta}^2 \widehat{\bar{\rho}} \left \widehat{S} \right \widehat{S}_{ij} \right] \\ H_{ij} = \frac{\widehat{\Delta}^2 \widehat{\bar{\rho}} \widehat{g}_{ik} \widehat{g}_{jk}}{12} - \frac{\Delta^2}{12} \left[\widehat{\bar{\rho}} \widehat{g}_{ik} \widehat{g}_{jk} \right] \end{cases}$
D-WALE	$\langle \mathcal{L}_{ij} M_{ij} \rangle / \langle M_{ij} M_{ij} \rangle$	$M_{ij} = 2 \left[\Delta^2 \left(\widehat{\bar{\rho}} F_w(\widehat{\mathbf{g}}) \widetilde{S}_{ij} \right) - \widehat{\Delta}^2 \widehat{\bar{\rho}} F_w(\widehat{\mathbf{g}}) \widehat{S}_{ij} \right]$
D-Mod.Gradient	$\langle \mathcal{L}_{ij} M_{ij} \rangle / \langle M_{ij} M_{ij} \rangle$	$M_{ij} = 2 \left[\widehat{\Delta}^2 \widehat{\bar{\rho}} k_{SGS}(\widehat{\mathbf{g}}) \widehat{g}_{ij} / \widehat{g}_{kk} - \left(\Delta^2 \widehat{\bar{\rho}} k_{SGS}(\widehat{\mathbf{g}}) \left(\frac{\widehat{g}_{ij}}{\widehat{g}_{kk}} \right) \right) \right]$

Table 5
Expressions for the dynamic coefficients.

Staffelbach) at CERFACS for their support and for giving access to their solver AVBP during the course of the project EDGES.

A. Dynamic constants

In Table 5 are gathered the explicit expressions for the dynamic coefficients of the different models studied. For all five models, the resolved stress tensor \mathcal{L}_{ij} from (31) is common. The coefficient for the Vreman model is presented in equation (40), where $\check{\nu}$ is the kinematic viscosity reconstructed from the filtered quantities using the EoS. Since it is not computed from the Germano's identity but from a transport equation for \mathcal{L}_{ij} , its expression is slightly different.

In the following, the notation $\widehat{(\cdot)}$ means that the quantity between the parentheses is filtered by the test filter.

$$C_d^{Vreman} = -\frac{\check{\nu}}{2} \frac{\langle \widehat{\bar{\rho}} \widehat{g}_{lm} \widehat{g}_{lm} - \widehat{\bar{\rho}} \widehat{g}_{lm} \widehat{g}_{lm} \rangle}{\langle \left(\widehat{\bar{\rho}} F_v(\widehat{\mathbf{g}}) \widetilde{S}_{lm} \widetilde{S}_{lm} \right) - \widehat{\bar{\rho}} F_v(\widehat{\mathbf{g}}) \widehat{S}_{lm} \widehat{S}_{lm} \rangle} \quad (40)$$

B. Comparison of t_{xy} in the (x, y) plane

For the sake of completeness and to further compare the models with the DNS, arbitrary 2D planar cuts, colored by t_{xy} normalized by its variance, are considered in Figures 9-16. These results overall illustrate the conclusions drawn in this study. Gradient models tend to better locate the positive or negative regions thereby achieving better correlation levels. Yet eddy viscosity models tend to better reproduce the size and amplitudes of the characteristic structures shaped by the fluctuations of t_{xy} . Adding a dynamic procedure tends to improve the results especially for the PG case. In the RG case however, eddy viscosity models do not perform as well as in the PG case. This fact can be associated to these models having difficulties reproducing the size of the structures shaped by t_{ij} . As for the PG case, gradient based models also struggle predicting the right amplitude for t_{ij} fluctuations. In the RG case, the dynamic strategy does not seem as adequate as in the PG case and results are still not satisfactory.

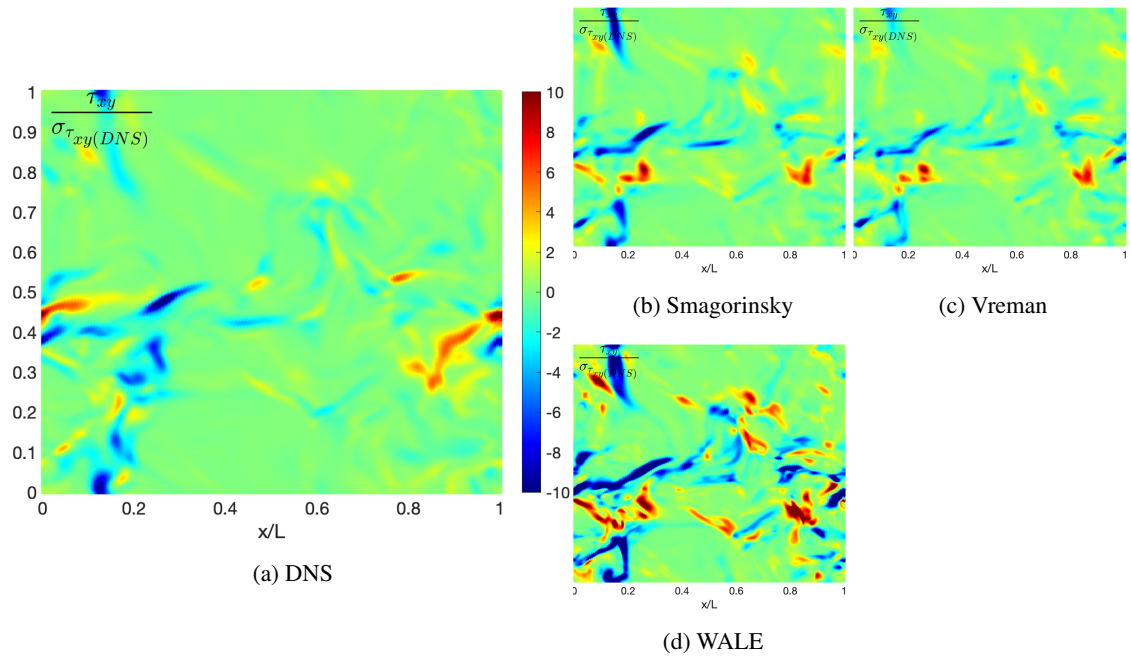


Figure 9: t_{xy} normalized by its variance in the (x, y) plane. PG case. Turbulent SGS viscosity models.

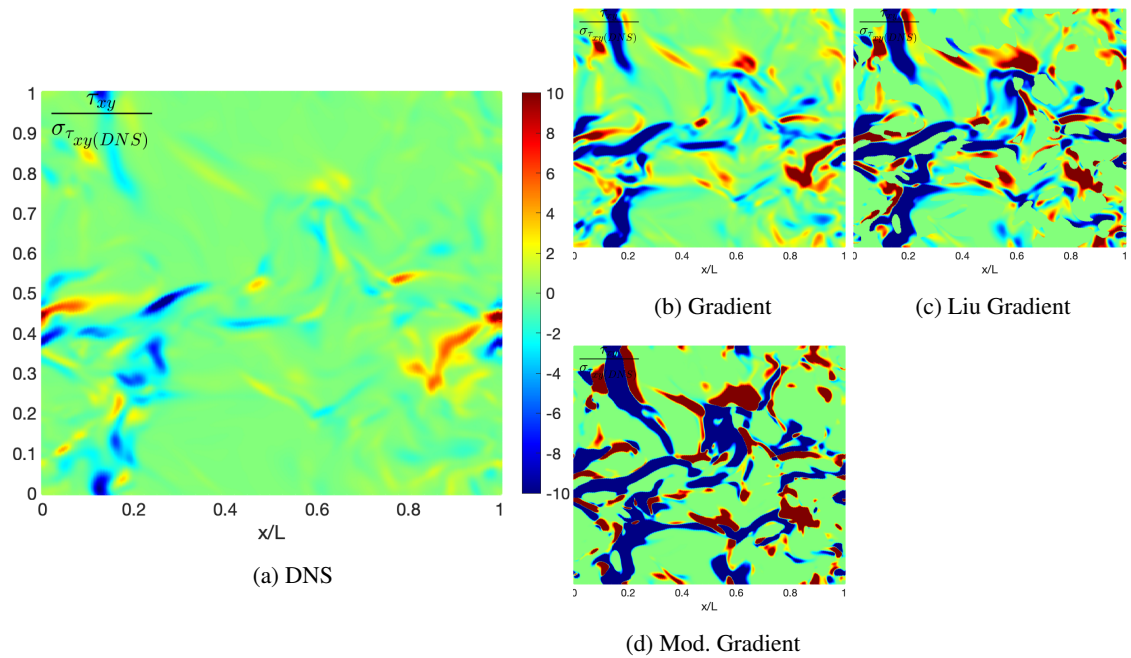


Figure 10: t_{xy} normalized by its variance in the (x, y) plane. PG case. Gradient models.

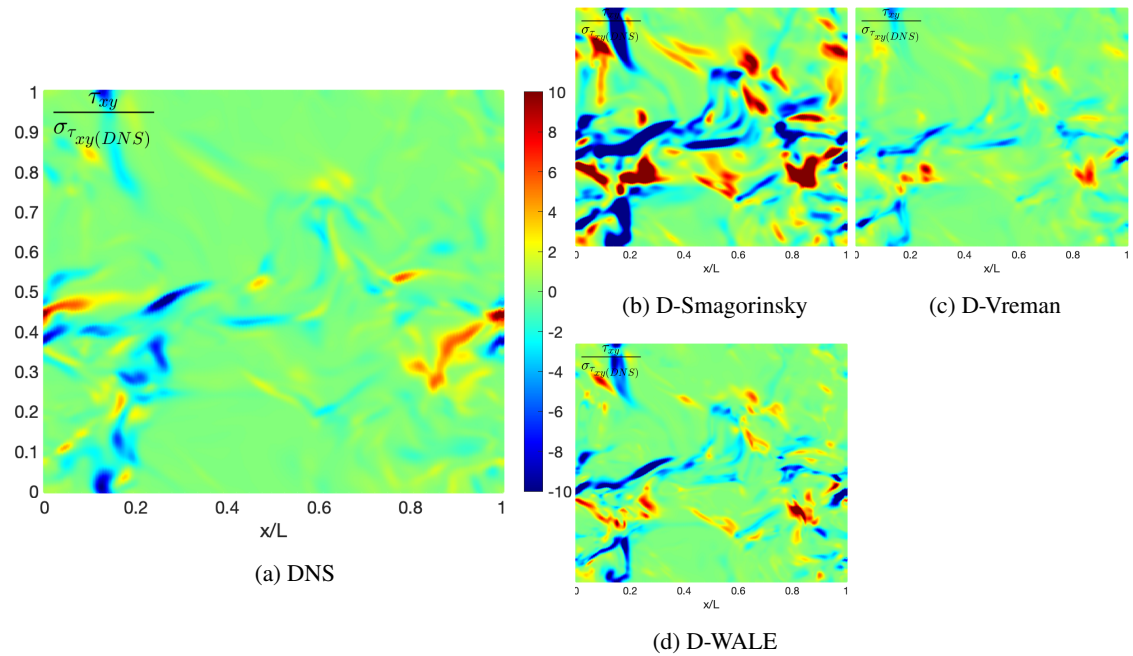


Figure 11: t_{xy} normalized by its variance in the (x, y) plane. PG case. Dynamic turbulent SGS viscosity models.

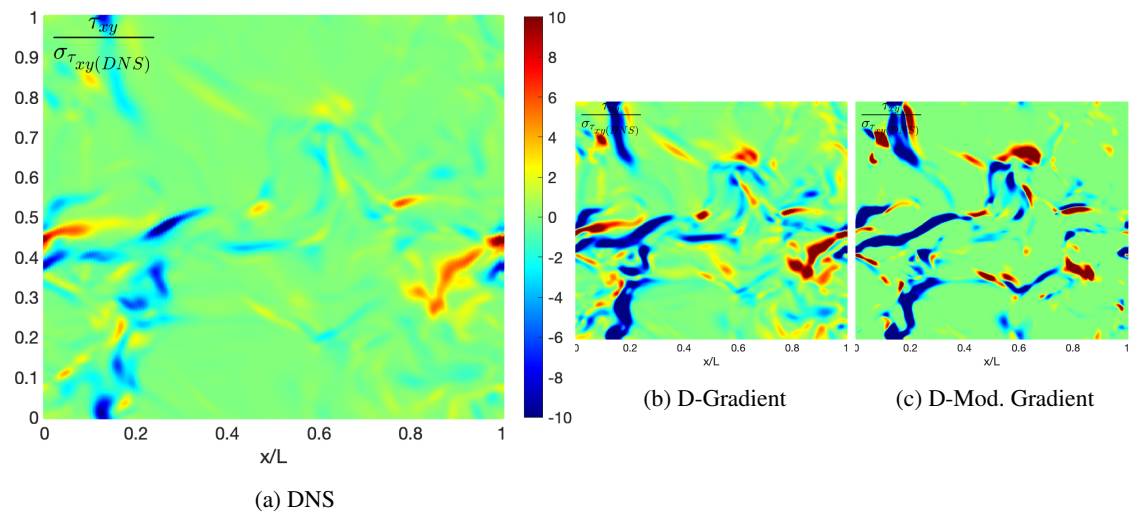


Figure 12: t_{xy} normalized by its variance in the (x, y) plane. PG case. Dynamic gradient models.

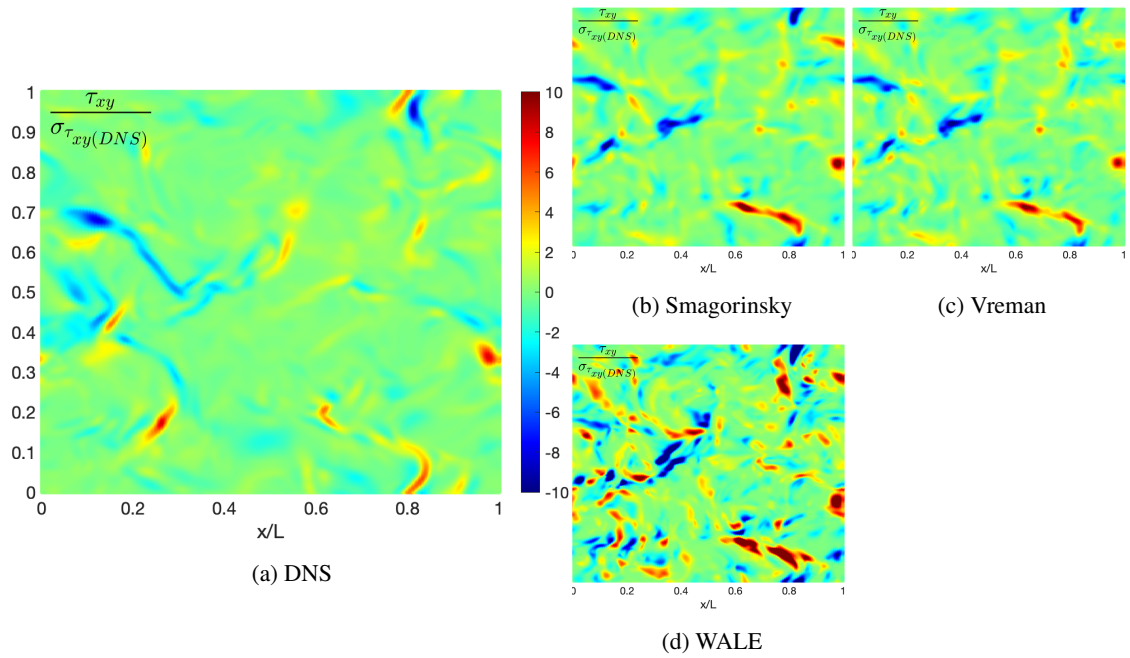


Figure 13: t_{xy} normalized by its variance in the (x, y) plane. RG case. Turbulent SGS viscosity models.

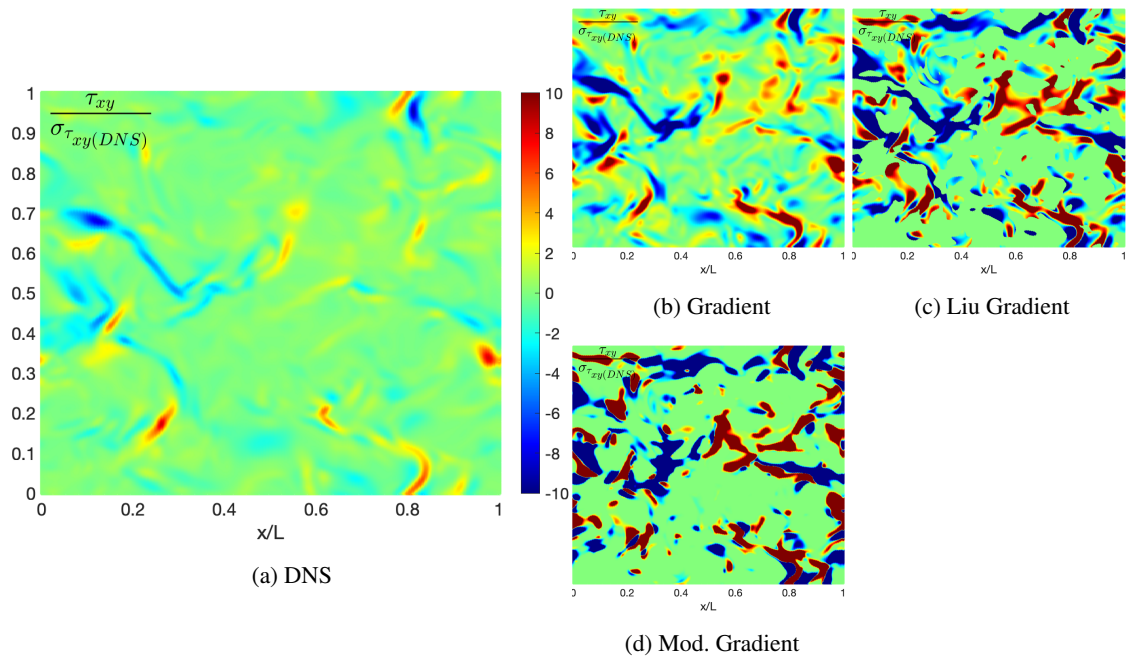


Figure 14: t_{xy} normalized by its variance in the (x, y) plane. RG case. Gradient models.

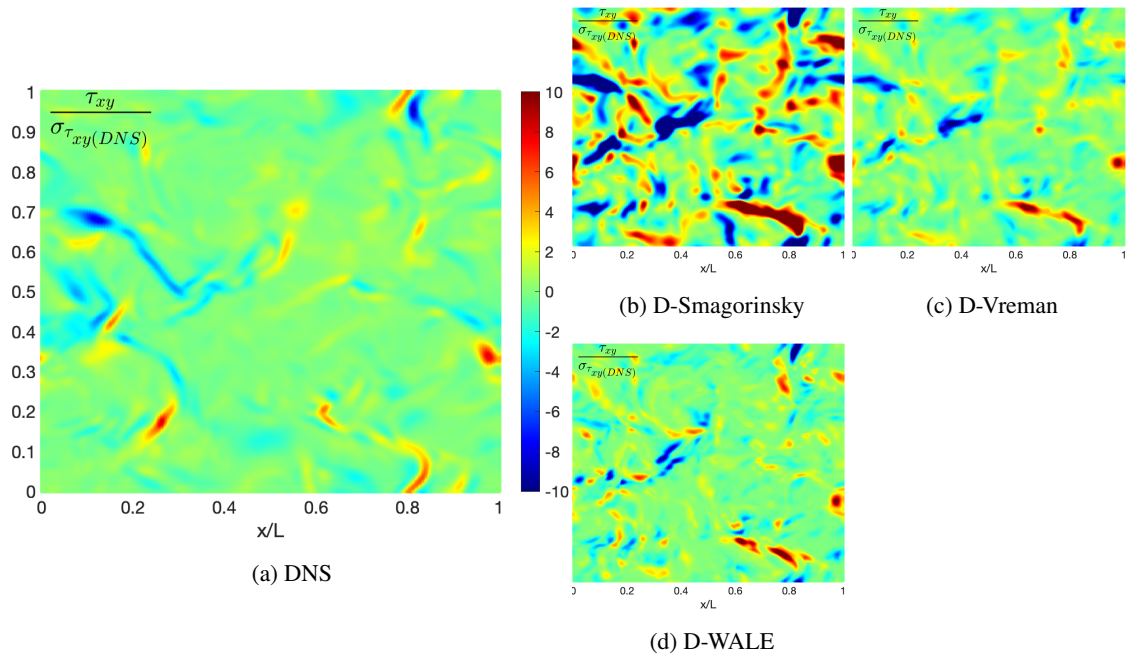


Figure 15: t_{xy} normalized by its variance in the (x, y) plane. RG case. Dynamic turbulent SGS viscosity models.

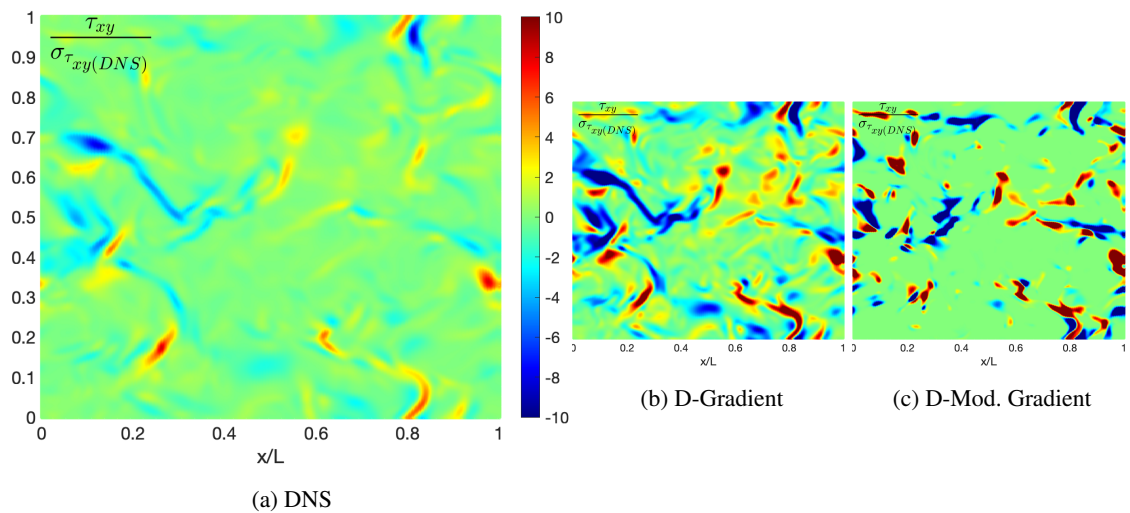


Figure 16: t_{xy} normalized by its variance in the (x, y) plane. RG case. Dynamic gradient models.

C. Chung et al. [40] Transport coefficients model

In order to take into account dense-gas effects, the dense-gas viscosity μ is written as the sum of two terms:

$$\mu = \mu_k + \mu_p \quad (41)$$

where μ_k a modified dilute-gas viscosity and μ_p a correction term. Chung et al. [40] prescribe that

$$\mu_k = \mu_0 \left[\frac{1}{G} + A_6 Y \right] \quad (42)$$

$$\mu_p = 36.44 \times 10^{-6} \frac{(MT_c)^{1/2}}{v_c^{2/3}} A_7 Y^2 \text{Exp} [A_8 + A_9 (T^*)^{-1} + A_{10} (T^*)^{-2}] \quad (43)$$

$$\text{and } \mu_0 = 40.785 \frac{F_c (MT)^{1/2}}{v_c^{2/3} \Omega_v} \quad (44)$$

where M is the molecular weight, T the temperature, T_c the critical temperature, v_c the critical volume and all inner parameters such as $A_{6...10}$, F_c , G , T^* , Y , and Ω_v can be directly computed using the relations detailed in [40]. Using the same approach as for viscosity, the dense-gas thermal conductivity κ is computed as:

$$\kappa = \kappa_k + \kappa_p \quad (45)$$

with

$$\kappa_k = \kappa_0 \left[\frac{1}{H} + B_6 Y \right] \quad (46)$$

$$\kappa_p = 3.039 \times 10^{-4} \sqrt{\frac{T}{M}} \frac{1}{v_c^{2/3}} B_7 Y^2 H \quad (47)$$

The dilute-gas component κ_0 is written as

$$\kappa_0 = 7.452 \frac{\mu_0 \Psi_\kappa}{M} \quad (48)$$

The reader is referred to [40] for the computation of the parameters H , $B_{6,7}$ and Ψ_κ .

D. Martin & Hou [42] Equation of State

The calorific and thermal Martin & Hou (MH) EoS are used in this study:

$$p = \frac{RT}{v-b} + \sum_{i=2}^5 \frac{A_i + B_i T + C_i e^{-kT/T_c}}{(v-b)^i} \quad (49)$$

$$E_{int} = E_{int,ref} + \int_{T_{ref}}^T c_v(T') dT' + \sum_{i=2}^5 \frac{A_i + C_i (1 + kT/T_c) e^{-kT/T_c}}{(i-1)(v-b)^{(i-1)}}$$

with $b = v_c(1 - (-31.888Z_c + 20.533)/15)$, $k = 5.475$. Z_c is the compressibility factor, T_c and v_c are the critical temperature and critical specific volume, respectively and the notation $(\cdot)_{ref}$ refers to the reference state.

Using data summarized in Table 1, the numerical constants A_i , B_i , C_i are computed following equations 50 to 58.

$$C_2 = \frac{\left(f_2 + bRT_p + (RT_p)^2 \frac{1-Z_c}{P_c} \right) (T_b - T_c) + (f_2 + bRT_b)(T_c - T_p)}{(T_b - T_c) (e^{-k} - e^{[-kT_p/T_c]}) - (T_c - T_p) (e^{[-kT_b/T_c]} - e^{-k})} \quad (50)$$

$$B_2 = \frac{-f_2 - bRT_b - C_2 (e^{[-kT_b/T_c]} - e^{-k})}{T_b - T_c} \quad (51)$$

$$C_3 = C_2 \frac{(v_c - b)^3 - (v_c/2 - b)^3}{(v_c/2 - b)^2 - (v_c - b)^2} \quad (52)$$

$$C_5 = -C_2(v_c - b)^3 - C_3(v_c - b)^2 \quad (53)$$

$$A_2 = f_2 - B_2 T_c - C_2 e^{-k} \quad (54)$$

$$A_4 = f_4 \quad (55)$$

$$B_5 = \frac{f_5 - C_5 e^{-k}}{T_c} \quad (56)$$

$$B_3 = m(v_c - b)^3 - R(v_c - b)^2 - B_2(v_c - b) - \frac{B_5}{(v_c - b)^2} \quad (57)$$

$$A_3 = f_3 - B_3 T_c - C_3 e^{-k} \quad (58)$$

where

$$f_2 = 9P_c(v_c - b)^2 - 3.8RT_c(v_c - b)$$

$$f_3 = 5.4RT_c(v_c - b)^2 - 17P_c(v_c - b)^3$$

$$f_4 = 12P_c(v_c - b)^4 - 3.4RT_c(v_c - b)^3$$

$$f_5 = 0.8RT_c(v_c - b)^4 - 3P_c(v_c - b)^5$$

The variables T_p and m can be computed following the procedure proposed by Martin & Hou [42].

References

- [1] J. Smagorinsky, General circulation experiments with the primitive equations: I. the basic experiment, *Monthly weather review* 91 (1963) 99–164.
- [2] J. W. Deardorff, et al., A numerical study of three-dimensional turbulent channel flow at large reynolds numbers, *J. Fluid Mech* 41 (1970) 453–480.
- [3] A. Leonard, Energy cascade in large-eddy simulations of turbulent fluid flows, in: *Advances in geophysics*, volume 18, Elsevier, 1975, pp. 237–248.
- [4] P. Moin, K. Mahesh, Direct numerical simulation: A tool in turbulence research, *Annual Review of Fluid Mechanics* 30 (1998) 539–578.
- [5] U. Piomelli, P. Moin, J. H. Ferziger, Model consistency in large eddy simulation of turbulent channel flows, *The Physics of fluids* 31 (1988) 1884–1891.
- [6] C. Meneveau, J. Katz, Scale-invariance and turbulence models for large-eddy simulation, *Annual Review of Fluid Mechanics* 32 (2000) 1–32.
- [7] F. Di Mare, W. Jones, K. Menzies, Large eddy simulation of a model gas turbine combustor, *Combustion and Flame* 137 (2004) 278–294.
- [8] A. Giauque, L. Selle, L. Gicquel, T. Poinso, H. Buechner, P. Kaufmann, W. Krebs, System identification of a large-scale swirled partially premixed combustor using LES and measurements, *Journal of Turbulence* 6 (2005) N21.
- [9] P. Wolf, G. Staffelbach, L. Y. Gicquel, J.-D. Müller, T. Poinso, Acoustic and large eddy simulation studies of azimuthal modes in annular combustion chambers, *Combustion and Flame* 159 (2012) 3398–3413.
- [10] F. D. Galiana, A. Wheeler, J. Ong, C. de M Ventura, The effect of dense gas dynamics on loss in orc transonic turbines, in: *Journal of Physics: Conference Series*, volume 821:1, IOP Publishing, p. 012021.
- [11] C. Lagarza-Cortés, J. Ramírez-Cruz, M. Salinas-Vázquez, W. Vicente-Rodríguez, J. M. Cubos-Ramírez, Large-eddy simulation of transcritical and supercritical jets immersed in a quiescent environment, *Physics of Fluids* 31 (2019) 025104.
- [12] W.-S. Hwang, B.-K. Sung, W. Han, K. Y. Huh, B. J. Lee, H. S. Han, C. H. Sohn, J.-Y. Choi, Real-gas-flamelet-model-based numerical simulation and combustion instability analysis of a gh2/lox rocket combustor with multiple injectors, *Energies* 14 (2021) 419.
- [13] J.-C. Hoarau, P. Cinnella, X. Gloerfelt, Large eddy simulations of strongly non-ideal compressible flows through a transonic cascade, *Energies* 14 (2021) 772.
- [14] A. Giauque, C. Corre, M. Menghetti, Direct numerical simulations of homogeneous isotropic turbulence in a dense gas, in: *Journal of Physics: Conference Series*, volume 821:1, IOP Publishing, p. 012017.
- [15] A. Vadrot, A. Giauque, C. Corre, Analysis of turbulence characteristics in a temporal dense gas compressible mixing layer using direct numerical simulation, *Journal of Fluid Mechanics* 893 (2020).
- [16] A. Vadrot, A. Giauque, C. Corre, Direct Numerical Simulations of temporal compressible mixing layers in a BZT Dense Gas: influence of the convective Mach number, *Journal of Fluid Mechanics* (2021).
- [17] L. Duan, Q. Zheng, Z. Jiang, J. Wang, Dense gas effect on small-scale structures of compressible isotropic turbulence, *Physics of Fluids* 33 (2021) 115113.
- [18] T. Schmitt, Large-eddy simulations of the mascotte test cases operating at supercritical pressure, *Flow, Turbulence and Combustion* (2020) 1–31.
- [19] C. Zhang, Z. Yuan, L. Duan, Y. Wang, J. Wang, Dynamic iterative approximate deconvolution model for large-eddy simulation of dense gas compressible turbulence, *Physics of Fluids* 34 (2022) 125103.

- [20] A. Giauque, A. Vadrot, P. Errante, C. Corre, A priori analysis of subgrid-scale terms in compressible transcritical real gas flows, *Physics of Fluids* 33 (2021) 085126.
- [21] E. Garnier, N. Adams, P. Sagaut, *Large Eddy Simulation for Compressible Flows*, Springer Netherlands, 2009.
- [22] B. Vreman, B. Geurts, H. Kuerten, A priori tests of large eddy simulation of the compressible plane mixing layer, *Journal of engineering mathematics* 29 (1995) 299–327.
- [23] B. Vreman, B. Geurts, H. Kuerten, Subgrid-modelling in LES of compressible flow, *Applied scientific research* 54 (1995) 191–203.
- [24] M. P. Martin, U. Piomelli, G. V. Candler, Subgrid-scale models for compressible large-eddy simulations, *Theoretical and Computational Fluid Dynamics* 13 (2000) 361–376.
- [25] D. Dupuy, A. Toutant, F. Bataille, A priori tests of subgrid-scale models in an anisothermal turbulent channel flow at low mach number, *International Journal of Thermal Sciences* 145 (2019) 105999.
- [26] R. A. Clark, J. H. Ferziger, W. C. Reynolds, Evaluation of subgrid-scale models using an accurately simulated turbulent flow, *Journal of Fluid Mechanics* 91 (1979) 1–16.
- [27] J. Bardina, J. H. Ferziger, W. Reynolds, Improved subgrid-scale models for large-eddy simulation., *AIAA Paper* (1980).
- [28] Z. Wang, K. Luo, D. Li, J. Tan, J. Fan, Investigations of data-driven closure for subgrid-scale stress in large-eddy simulation, *Physics of Fluids* 30 (2018).
- [29] Z. Zhou, G. He, S. Wang, G. Jin, Subgrid-scale model for large-eddy simulation of isotropic turbulent flows using an artificial neural network, *Computers and Fluids* 195 (2019) 104319.
- [30] A. Prat, T. Sautory, S. Navarro-Martinez, A Priori Sub-grid Modelling Using Artificial Neural Networks, *International Journal of Computational Fluid Dynamics* 0 (2020) 1–21.
- [31] M. Germano, U. Piomelli, P. Moin, W. H. Cabot, A dynamic subgrid-scale eddy viscosity model, *stun* (1990) 5–17.
- [32] B. Vreman, B. Geurts, H. Kuerten, On the formulation of the dynamic mixed subgrid-scale model, *Physics of Fluids* 6 (1994) 4057–4059.
- [33] Y. Zang, R. L. Street, J. R. Koseff, A dynamic mixed subgrid-scale model and its application to turbulent recirculating flows, *Physics of Fluids A* 5 (1993) 3186–3196.
- [34] F. Nicoud, F. Ducros, Subgrid-scale stress modelling based on the square of the velocity gradient tensor, *Flow, Turbulence and Combustion* 62 (1999) 183–200.
- [35] F. Nicoud, H. B. Toda, O. Cabrit, S. Bose, J. Lee, Using singular values to build a subgrid-scale model for large eddy simulations, *Physics of Fluids* 23 (2011).
- [36] A. W. Vreman, An eddy-viscosity subgrid-scale model for turbulent shear flow: Algebraic theory and applications, *Physics of Fluids* 16 (2004) 3670–3681.
- [37] S. Liu, C. Meneveau, J. Katz, On the properties of similarity subgrid-scale models as deduced from measurements in a turbulent jet, *Journal of Fluid Mechanics* 275 (1994) 83–119.
- [38] H. Lu, F. Porté-Agel, A modulated gradient model for large-eddy simulation: Application to a neutral atmospheric boundary layer, *Physics of Fluids* 22 (2010) 015109.
- [39] A. Giauque, C. Corre, A. Vadrot, Direct numerical simulations of forced homogeneous isotropic turbulence in a dense gas, *Journal of Turbulence* 21 (2020) 186–208.
- [40] T. H. Chung, M. Ajlan, L. L. Lee, K. E. Starling, Generalized multiparameter correlation for nonpolar and polar fluid transport properties, *Industrial & Engineering Chemistry Research* 27 (1988) 671–679.
- [41] W. Sutherland, LII. the viscosity of gases and molecular force, *The London, Edinburgh, and Dublin Philosophical Magazine and Journal of Science* 36 (1893) 507–531.
- [42] J. J. Martin, Y.-C. Hou, Development of an equation of state for gases, *AICHE Journal* 1 (1955) 142–151.
- [43] J. J. Martin, R. M. Kapoor, N. D. Nevers, An improved equation of state for gases, *AICHE Journal* 5 (1959) 159–160.
- [44] L. C. Selle, N. A. Okong'o, J. Bellan, K. G. Harstad, Modelling of subgrid-scale phenomena in supercritical transitional mixing layers: an a priori study, *Journal of Fluid Mechanics* 593 (2007) 57–91.
- [45] E. S. Taşkınoğlu, J. Bellan, Subgrid-scale models and large-eddy simulation of oxygen stream disintegration and mixing with a hydrogen or helium stream at supercritical pressure, *Journal of Fluid Mechanics* 679 (2011) 156–193.
- [46] M. S. Cramer, Negative nonlinearity in selected fluorocarbons, *Physics of Fluids A: Fluid Dynamics* 1 (1989) 1894–1897.
- [47] T. Schönfeld, M. Rudgyard, Steady and Unsteady Flow Simulations Using the Hybrid Flow Solver AVBP, *AIAA Journal* 37 (1999) 1378–1385.
- [48] O. Colin, M. Rudgyard, Development of High-Order TaylorGalerkin Schemes for LES, *Journal of Computational Physics* 162 (2000) 338–371.
- [49] J. Boussinesq, *Essai sur la théorie des eaux courantes*, volume XXIII, Imprimerie nationale, Paris, 1877. Mémoires présentés par divers savants à l'Académie des sciences de l'Institut de France.
- [50] A. Leonard, Energy cascade in large-eddy simulations of turbulent fluid flows, in: *Turbulent Diffusion in Environmental Pollution*, Proceedings of a Symposium held at Charlottesville, Elsevier, 1974, pp. 237–248.
- [51] M. D. Love, Subgrid modelling studies with burgers' equation, *Journal of Fluid Mechanics* 100 (1980) 87.
- [52] B. Vreman, B. Geurts, H. Kuerten, Theoretical and computational fluid dynamics large-eddy simulation of the temporal mixing layer using the clark model, *Theoret. Comput. Fluid Dynamics* 8 (1996) 309–324.
- [53] M. Germano, U. Piomelli, P. Moin, W. Cabot, A dynamic subgrid-scale eddy viscosity model, *Physics of Fluids A* 3 (1991) 1760–1765.
- [54] M. Germano, A proposal for a redefinition of the turbulent stresses in the filtered navier–stokes equations, *Physics of Fluids* 29 (1986) 2323.
- [55] C. G. Speziale, Galilean invariance of subgrid-scale stress models in the large-eddy simulation of turbulence, *Journal of Fluid Mechanics* 156 (1985) 55.
- [56] D. Lilly, A proposed modification of the germano subgrid-scale closure method, *Physics of Fluids A* 4 (1992) 633–635.
- [57] F. Nicoud, H. B. Toda, O. Cabrit, S. Bose, J. Lee, Using singular values to build a subgrid-scale model for large eddy simulations, *Physics of Fluids* 23 (2011).

- [58] H. Lu, F. Porté-Agel, On the development of a dynamic non-linear closure for large-eddy simulation of the atmospheric boundary layer, *Boundary-Layer Meteorology* 151 (2014) 429–451.
- [59] S. Singh, D. You, A dynamic global-coefficient mixed subgrid-scale model for large-eddy simulation of turbulent flows, *International Journal of Heat and Fluid Flow* 42 (2013) 94–104.
- [60] D. Baumgärtner, J. J. Otter, A. P. S. Wheeler, The Effect of Isentropic Exponent on Transonic Turbine Performance, *Journal of Turbomachinery* 142 (2020) 081007.